

# The enhancement of photo-oxidation efficiency of elemental mercury by immobilized WO<sub>3</sub>/TiO<sub>2</sub> at high temperatures



Huazhen Shen<sup>a</sup>, Iau-Ren Ie<sup>a</sup>, Chung-Shin Yuan<sup>a,\*</sup>, Chung-Huang Hung<sup>b</sup>

<sup>a</sup> Institute of Environmental Engineering, National Sun Yat-Sen University, No. 70, Lian-Hai Road, Kaohsiung 804, Taiwan

<sup>b</sup> Department of Safety, Health and Environmental Engineering, National Kaohsiung First University of Science and Technology, No. 2, Juoyue Road, Kaohsiung 811, Taiwan

## ARTICLE INFO

### Article history:

Received 20 July 2015

Received in revised form 15 January 2016

Accepted 22 April 2016

Available online 6 May 2016

### Keywords:

Photo-oxidation of Hg<sup>0</sup>

WO<sub>3</sub>/TiO<sub>2</sub>

Immobilized glass beads

L-H model

Equilibrium constant

## ABSTRACT

This study demonstrates the high photo-oxidation efficiencies of elemental mercury (Hg<sup>0</sup>) at high temperatures (120, 140, 160 °C) by WO<sub>3</sub>/TiO<sub>2</sub>. The photocatalysts TiO<sub>2</sub>(sol-gel) and 1–7% WO<sub>3</sub>/TiO<sub>2</sub> prepared by sol-gel synthesis are immobilized on the surfaces of glass beads. The form of doped WO<sub>3</sub> is characterized by SEM, HRTEM, XRD, Raman, PL, XPS, UV–vis spectrum and BET specific surface area analysis, respectively. The effects of gaseous pollutants in the flue gases emitted from coal-fired power plants, including HCl, NO, SO<sub>2</sub>, CO<sub>2</sub> and H<sub>2</sub>O, are investigated as regards the photo-oxidation efficiency of Hg<sup>0</sup>. The experimental results indicate that the highest Hg<sup>0</sup> photo-oxidation efficiency is achieved by TiO<sub>2</sub> doped with 1–3% WO<sub>3</sub>, which result in a 4-fold increase in the Hg<sup>0</sup> photo-oxidation efficiency, as compared with TiO<sub>2</sub>. Simulated by the Langmuir–Hinshelwood model and thermodynamics analysis for Hg<sup>0</sup> photo-oxidation, the equilibrium constant ( $K_{\text{Hg}^0}$ ) and the change of Gibbs free energy ( $\Delta G$ ) are determined for the various photocatalysts. The enhancement of the Hg<sup>0</sup> photo-oxidation efficiency is mainly attributed to the increase of  $K_{\text{Hg}^0}$  for WO<sub>3</sub>/TiO<sub>2</sub> at high temperatures, as compared with TiO<sub>2</sub>(DegussaP25) and TiO<sub>2</sub>(sol-gel). This study further reveals that SO<sub>2</sub>, NO and H<sub>2</sub>O inhibit the photo-oxidation efficiency of Hg<sup>0</sup>, but that it is enhanced by HCl.

© 2016 Elsevier B.V. All rights reserved.

## 1. Introduction

Due to its severe adverse effects on human health, elemental mercury (Hg<sup>0</sup>) and its derivatives released from industrial sources are of concern for both governments and non-governmental organizations (NGOs) worldwide. There are several industrial sources contributing to the release of Hg into the environment [1,2], and the gaseous elemental mercury (Hg<sup>0</sup>) emitted from coal-fired power plants has been restricted in order to meet air quality standards in every country [3]. In particular, in 2013, the Minamata Convention resulted in signed agreements to regulate Hg<sup>0</sup> emissions [4]. However, it is still necessary to develop more efficient Hg<sup>0</sup> removal processes in order to further reduce the emission of Hg<sup>0</sup>.

Studies regarding Hg<sup>0</sup> emission control technology have been conducted for many years, and have included such topics as adsorption, absorption, thermal-oxidation and photo-oxidation [3]. Due

to a higher removal efficiency [5,6] and lower cost than for activated carbon adsorption, the photo-oxidation of Hg<sup>0</sup> by TiO<sub>2</sub> has been demonstrated to be an excellent process. However, there are still some difficulties in directly applying TiO<sub>2</sub>-assisted photocatalytic oxidation processes to the removal of mercury from the gas streams of coal-fired power plants in high-temperature environments (>100 °C) [6]. The temperature of the gas streams of coal-fired power plants, after being treated with ESP, ranges from 100 to 180 °C [7], causing a reduction in the photo-oxidation efficiency of Hg<sup>0</sup> [8,9].

Previous literatures regarding the application of TiO<sub>2</sub> based materials to Hg<sup>0</sup> removal usually focused on the ambient temperature at which Hg<sup>0</sup> was efficiently removed by TiO<sub>2</sub> under near-UV irradiation. For example, Cho investigated that at ambient temperature the effects of the irradiation wave number, irradiation strength, the gas components (HCl, SO<sub>2</sub>, NO, H<sub>2</sub>O etc.), Hg<sup>0</sup> concentrations, and etc on the photo-oxidation efficiency of Hg<sup>0</sup> by TiO<sub>2</sub> [10,11]. In addition, the improvements of photo-catalytic reactivity of modified TiO<sub>2</sub> under visible light irradiation at an ambient temperature were also investigated widely, such as the perfor-

\* Corresponding author.

E-mail address: [ycsngi@mail.nsysu.edu.tw](mailto:ycsngi@mail.nsysu.edu.tw) (C.-S. Yuan).

mances of  $\text{Al}_2\text{O}_3/\text{TiO}_2$  [12],  $\text{CuO}/\text{TiO}_2$  [13,14] and etc. The enhanced photo-oxidation efficiency can be attributed to the generation of photo-induced electrons and holes due to the hybrid band structure in modified  $\text{TiO}_2$  crystal when irradiated with visible light, of which energy is lower than the band gap of  $\text{TiO}_2$ . Wu et al. reported under irradiation of visible light, the enhanced photo-oxidation efficiency of  $\text{Hg}^0$  by  $\text{CuO}/\text{TiO}_2$  was not only resulted from the narrowness of band gap but also the prevention of the combination of photo-induced electrons and holes by adding  $\text{CuO}$  [13]. However, the investigations on the photo-oxidation of  $\text{Hg}^0$  at relatively higher temperatures ( $>100^\circ\text{C}$ ) by  $\text{TiO}_2$  were rarely explored. Therefore, it's necessary to investigate the photo-catalytic reactivity and performance of  $\text{TiO}_2$  and modified  $\text{TiO}_2$  at higher temperatures simulating the environment of coal-fired power plants.

The photo-catalytic reactivity of Degussa P25 for  $\text{Hg}^0$  removal at high temperatures has been investigated [15], and the reduction of photo-oxidation efficiency was caused by the elevation of temperatures above  $140^\circ\text{C}$  for Degussa P25. Therefore, the motivation to improve the photo-reactivity of Degussa P25 was to allow it to sustain a high efficiency even if the environment temperatures were not suitable for the photo-oxidation process. Accordingly, to overcome the low reactivity of  $\text{TiO}_2$  in high-temperature environments, many research efforts have focused on the modification of  $\text{TiO}_2$ -based photocatalysts in order to change the band gap and prolong the separation time of photo-induced electrons and holes. Of the different metal oxide modifications,  $\text{WO}_3$  has received considerable attention due to its optical and electrochromic properties [16].  $\text{WO}_3$  modified  $\text{TiO}_2$  has been applied in various areas, such as the production of an electrical capacitor with huge energy storage [17]. The addition of  $\text{WO}_3$  to SCR catalysts can improve resistance towards high temperatures and alkali salts [18,19]. For the removal of  $\text{Hg}^0$  especially, the enhancement by  $\text{WO}_x/\text{TiO}_2$  has been demonstrated to achieve a high efficiency of 100% at  $135^\circ\text{C}$  as a result of prolonging the separation time of the photo-induced electrons and holes [20].

Many methods have been used in an attempt to modify  $\text{TiO}_2$  as a more efficient photocatalyst, such as thermal plasma methods [12,21], electrospinning methods [22], the sol-gel method [23,24] and transitional metal oxide doping into Degussa P25 [25–27]. However, the immobilization of modified powdery  $\text{TiO}_2$  seems to be problematic insofar as confining the application to air pollution control research. The chemical vapor deposition [28] and vacuum sputtering deposition methods [29,30] provide a uniform coating, but their high cost restricts their potential application. The immobilization of modified Degussa P25 is an easy and cost-saving approach, but the effects of doping into Degussa P25 are uncertain. To the best of our knowledge, there are few reports on the immobilization of sol-gel modified  $\text{TiO}_2$  or on the application of the immobilization of sol-gel photocatalysts to the photo-oxidation of  $\text{Hg}^0$ .

Accordingly, this study involved the preparation of  $\text{WO}_3/\text{TiO}_2$  composite photocatalysts using sol-gel methods and an investigation of their contribution to the photo-oxidation of  $\text{Hg}^0$  at high temperatures. Characterization tests for the prepared photocatalysts were evaluated with SEM, TEM, BET, XRD, UV–vis spectrum, Raman, XPS and PL. The amount of  $\text{WO}_3$  doped on  $\text{TiO}_2$  for  $\text{Hg}^0$  photo-oxidation was investigated. The effects of reaction temperatures ranging from  $120$  to  $160^\circ\text{C}$  on the photo-oxidation efficiencies of  $\text{Hg}^0$  were also investigated. In addition, both the L-H model and thermodynamic analysis were performed to elucidate the reaction mechanisms for increasing photo-oxidation efficiency of  $\text{Hg}$  by  $\text{TiO}_2$  doped with  $\text{WO}_3$ . Finally, other gaseous components, including  $\text{HCl}$ ,  $\text{NO}$ ,  $\text{SO}_2$ ,  $\text{CO}_2$  and  $\text{H}_2\text{O}$ , were tested for their effects on the photo-oxidation efficiencies of  $\text{Hg}^0$  in typical flue gases emitted from coal-fired power plants.

## 2. Experiments

### 2.1. Preparation of photocatalysts

The photocatalysts used for this study were prepared by coating calcinated  $\text{TiO}_2$  onto the surface of 2.6 mm glass beads with a surface area of  $0.010\text{ m}^2/\text{g}$ . The glass beads were first rinsed separately in sodium hydroxide and sulfuric acid solutions to clean their surfaces, and then they were rinsed with DI water and dried in an oven at  $105^\circ\text{C}$  prior to coating. The photocatalysts immobilized on the surface of the glass beads included Degussa P25,  $\text{TiO}_{2(\text{sol-gel})}$  and 1–7%  $\text{WO}_3/\text{TiO}_2$ , respectively. The immobilization of Degussa P25 followed the impregnation methods used in previous studies [15,31]. One gram of Degussa P25 was dissolved in 15 mL DI water and continuously stirred at  $60$ – $70^\circ\text{C}$  for 30 min. The slurry was then sprayed onto the surfaces of the heated glass beads. After being dried at  $105^\circ\text{C}$  for 30 min, the Degussa P25-coated glass beads were further heated for 3 h at  $500^\circ\text{C}$  of the optimal calcination temperature to improve the photocatalytic reactivity of Degussa P25 [15], denoted as  $\text{TiO}_{2(\text{DegussaP25})}$ .

The precursors of the sol-gel prepared  $\text{TiO}_2$  were isopropanol titanium (Acros Organics, USA), isopropanol (Shimakyu's Pure Chemicals, JP), acetic acid (Panreac, USA) and  $\text{H}_2\text{O}$  with a volume ratio of 1:2:2:3. Droplets of a mixture of isopropanol and acetic acid were dripped into the isopropanol titanium at a rate of three drops per second. Once the mixture of the reagent had been stirred continuously for 10 h at ambient temperature, it turned into sol, and then DI water was steadily added to it. The sol turned into gelatin when its temperature reached  $65$ – $70^\circ\text{C}$  by heating. It was then dried at  $105^\circ\text{C}$  for 10 h, calcinated at  $500^\circ\text{C}$  for 3 h and ground into the powder here denoted as  $\text{TiO}_{2(\text{sol-gel})}$ . The preparation of 1–7%  $\text{WO}_3/\text{TiO}_2$  followed the same procedure as the preparation of  $\text{TiO}_{2(\text{sol-gel})}$ , except that different concentrations of ammonium tungstate solution were added to the sol to prepare 1, 3, 5 and 7%  $\text{WO}_3/\text{TiO}_2$ , respectively. During the immobilization procedure, the slurry of the sol-gel photocatalyst powder, made up with a ratio of 1 g to 15 mL  $\text{H}_2\text{O}$ , was thoroughly mixed by means of ultrasonic vibration. The mixture was then coated onto the glass beads and dried at  $105^\circ\text{C}$ . The immobilization process was repeated until the glass beads were successfully coated with a sufficient amount of photocatalysts. The successfully immobilized photocatalyst is shown in Fig. S1.

### 2.2. Characterization of photocatalysts

The measurement of the BET specific surface area of the photocatalysts was carried out using a nitrogen adsorption instrument at  $77\text{ K}$  (Micrometrics, ASAP 2020). Each sample was outgassed at  $105^\circ\text{C}$  prior to the measurement of the specific surface area. The X-ray diffraction (XRD) pattern was detected with an X-ray Diffractometer (Siemens, D5000) using  $\text{CuK}\alpha$  radiation as the X-ray source. A scanning angle range was initiated from  $20^\circ$  to  $80^\circ$  with a step time of  $0.5^\circ/\text{s}$ . The diameters of the anatase and rutile in the  $\text{TiO}_2$  crystallite can be estimated by the Scherrer Equation:

$$D = \frac{0.89\lambda}{B\cos\theta} \quad (1)$$

where  $\lambda$  is the wavelength of  $1.54\text{ \AA}$ ;  $\theta$  is the diffraction angle; and  $B$  is the corrected half width of the crystal measured.

The mass fraction of anatase in the photocatalysts can be determined by Eq. (2) [32]:

$$f_A = \frac{1}{1 + 1.26(I_R/I_A)} \quad (2)$$

where  $I_R$  represents the intensity of rutile at  $2\theta = 27.46^\circ$ ; and  $I_A$  represents the intensity of anatase at  $2\theta = 25.36^\circ$ .

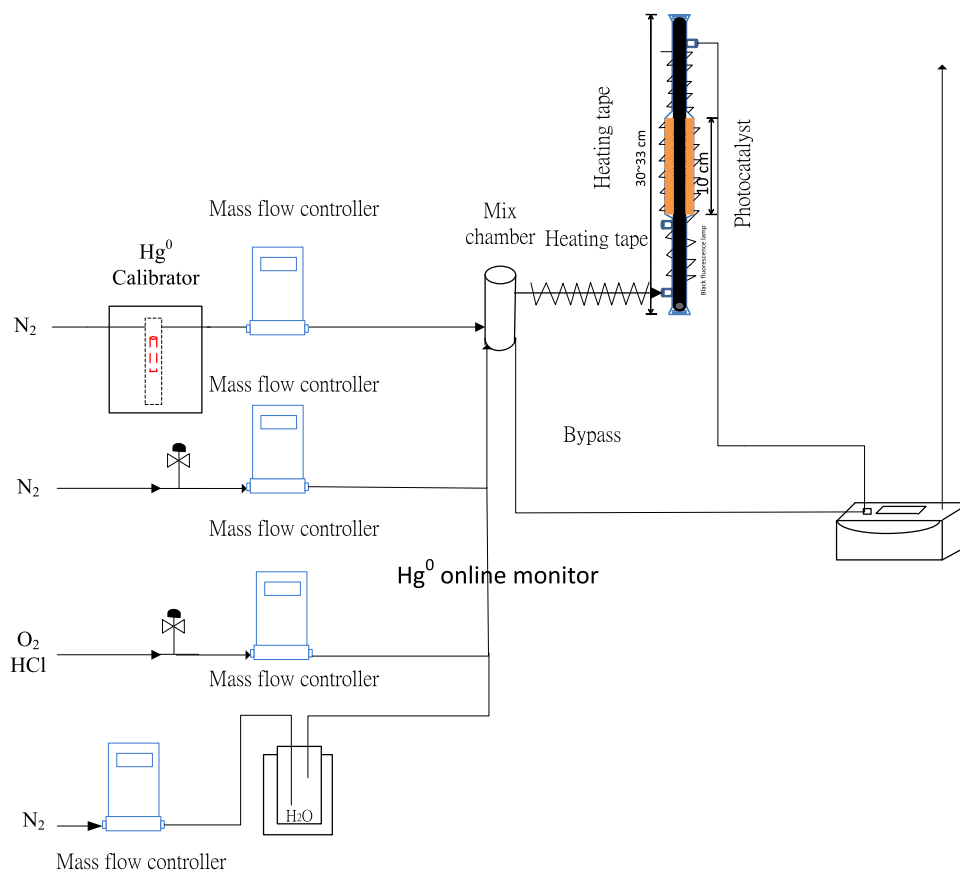


Fig. 1. The schematics of experimental set-up for the  $\text{Hg}^0$  photo-oxidation system.

**Table 1**  
Experimental condition for the photo-oxidation reaction of  $\text{Hg}^0$ .

	Photocatalysts	Reaction Temperature ( $^{\circ}\text{C}$ )	Influent Conc. $\text{Hg}^0$ ( $\mu\text{g}/\text{m}^3$ )	Gas Component
1	$\text{TiO}_2(\text{DegussaP25})$ , $\text{TiO}_2(\text{sol-gel})$ , 1–7% $\text{WO}_3/\text{TiO}_2$	160	25	$\text{N}_2$
2	$\text{TiO}_2(\text{DegussaP25})$ , $\text{TiO}_2(\text{sol-gel})$ , 1–7% $\text{WO}_3/\text{TiO}_2$	120, 140, 160	25, 50, 75, 100	$\text{N}_2$
3	$\text{TiO}_2(\text{sol-gel})$ , 1–5% $\text{WO}_3/\text{TiO}_2$	160	50	$\text{N}_2 + \text{HCl}$ , $\text{SO}_2$ , $\text{NO}$ , $\text{CO}_2$ , $\text{H}_2\text{O}$

**Table 2**  
The BET surface area and crystallite size of  $\text{TiO}_2(\text{DegussaP25})$ ,  $\text{TiO}_2(\text{sol-gel})$ , and 1–7% $\text{WO}_3/\text{TiO}_2$ .

Photocatalysts	BET Surface Area ( $\text{m}^2/\text{g}$ )	BJH Adsorption Cumulative Pore Volume ( $\text{cm}^3/\text{g}$ )	Mass Fraction of Anatase (%) $f = \frac{1}{1 + 1.26 \left( \frac{R_B}{R_A} \right)}$	Crystallite Size (nm)		Band Gap (eV)
				Anatase	Rutile	
$\text{TiO}_2(\text{DegussaP25})$	43.9	0.36	80	22	27	2.99
$\text{TiO}_2(\text{sol-gel})$	75.1	0.22	100	14	–	2.96
1% $\text{WO}_3/\text{TiO}_2$	76.6	0.21	99	13	–	3.06
3% $\text{WO}_3/\text{TiO}_2$	82.5	0.24	97	15	–	3.09
5% $\text{WO}_3/\text{TiO}_2$	82.8	0.21	95	13	–	3.10
7% $\text{WO}_3/\text{TiO}_2$	83.8	0.22	93	15	–	3.20

The morphologies of  $\text{TiO}_2(\text{DegussaP25})$ ,  $\text{TiO}_2(\text{sol-gel})$  and 1–7%  $\text{WO}_3/\text{TiO}_2$  were observed with a field-emission scanning electron microscopy (FESEM) (JEOL, 6330). Morphologies scanning was also performed using high resolution transmission electron microscopy (HRTEM) (JEOL, 3010). Samples were prepared by dispersing the photocatalysts in ethanol under ultrasonic vibration prior to deposition on a carbon-coated Cu grid.

The UV–vis adsorption spectra, ranging from 300 to 800 nm, were further determined with a Spectrophotometer (Perkin Elmer

Lambda 35, UV–λ35). The band gap can be calculated using the Kubelka–Munk Eq. (3):

$$\alpha h\nu = A(h\nu - E_g)^{n/2} \quad (3)$$

where  $\alpha$ ,  $\nu$ ,  $E_g$ , and  $A$  are the absorption coefficient (dimensionless), light frequency ( $\text{s}^{-1}$ ), band gap energy (eV), and a constant, respectively. For  $\text{TiO}_2$  and  $\text{WO}_3/\text{TiO}_2$ , the value of  $n$  is 4 for the indirect transition. The band gap was determined by extrapolating the linear portion of the  $(\alpha h\nu)^{1/2}$  versus the  $h\nu$  (eV) plot to zero absorption. The Raman spectra were recorded by an Horiba

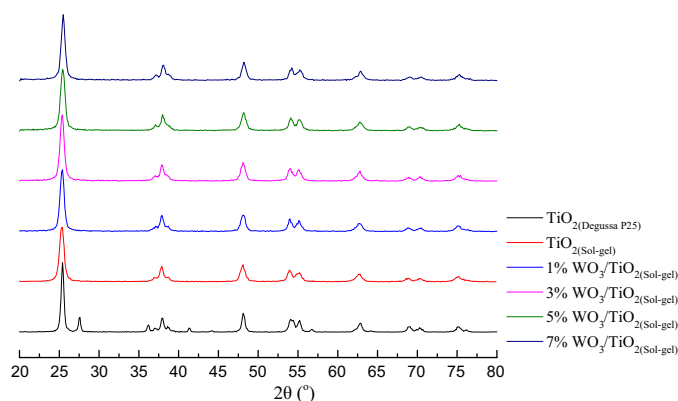


Fig. 2. The XRD patterns of  $\text{TiO}_2(\text{Degussa P25})$ ,  $\text{TiO}_2(\text{sol-gel})$ , and 1–7%  $\text{WO}_3/\text{TiO}_2$ .

HR800 Spectrometer and Jobin-Yvon Labram Aramis FT-Raman spectrophotometer. X-ray Photoelectron Spectroscopy (XPS) measurements were performed with an XPS system (VG Scientific, ESCALAB 250) at room temperature. A twin anode X-ray gun (600 W Al, 400 W Mg) was the X-ray source. The carbon 1s line (with binding energy of 284.8 eV) was used to calibrate the binding-energy scale of the XPS. To study the recombination of electrons and holes in the photocatalysts, the photoluminescence (PL) emission spectra of the photocatalysts were measured with the Horiba HR800 at room temperature, and a 325 nm He-Cd laser was used as an excitation light source.

### 2.3. Photo-oxidation of mercury

The schematics of the photo-oxidation experimental system is illustrated in Fig. 1. A dynacalibrator (VICI Metronics, Model 450) with an  $\text{Hg}^0$  permeation tube inside was used to generate  $\text{Hg}^0$ , which was then mixed with nitrogen gas. The overall influent flow was set as 850 mL/min, with a retention time of 0.69 s through calculation, and the flow ratios of the  $\text{Hg}^0$ -laden nitrogen and diluted nitrogen were controlled by mass flow controllers to obtain  $\text{Hg}^0$  concentrations of 0–100  $\mu\text{g}/\text{m}^3$ . A continuous cylindrical reactor, with length of 400 mm, diameter of 25 mm and a central cartridge of 100 mm in length and 35 mm in diameter, filled with photocatalyst-coated glass beads was positioned vertically. A lamp with a specific wavelength was placed in the middle of the photocatalytic reactor, leaving a slit to hold the photocatalyst-coated glass beads between the glass inner wall and the lamp. The lamp used in this study was a 365 nm black UV light with a power of 15 W. At the end of the photocatalytic reactor, the light was jacketed with rubber O-rings and plastic plugs to avoid  $\text{Hg}^0$  leakage from the end. The outer wall of the photocatalytic reactor was wrapped with heating tape to control the elevated temperatures using a K-type thermocouple touching the photocatalysts. The Teflon gas tube connecting the mixing chamber and the photocatalytic reactor was also pre-heated with a heating tape to avoid the condensation of water vapor. Through a mass flow controller, a single gas component, such as HCl,  $\text{SO}_2$ , NO,  $\text{CO}_2$  and  $\text{H}_2\text{O}$ , was mixed in a mixing chamber with the main stream containing  $\text{Hg}^0$ .

The loading weight of the photocatalysts onto the surface of the glass beads was about 0.2 g of photocatalyst per 20 g of glass beads, as determined by the weight difference of the glass beads before and after coating. The thickness of the coating film of the photocatalysts was about 9–10  $\mu\text{m}$ , equal to the volume of the photocatalyst divided by the surface areas of the glass beads. The amount of photocatalyst (Degussa P25) coated on 20 g of glass beads was 0.2 g, which was set in the photo-oxidation reactor for the experiments,

and reached up to 100% photo-oxidation efficiency of  $\text{Hg}^0$  at 100 °C in a previous study [15].

Water vapor was produced by heating a bottle containing deionized  $\text{H}_2\text{O}$  and laden with carrier gas  $\text{N}_2$  in the mixing chamber. The relative humidity (RH) was monitored online by means of an hygrometer in the mixing chamber. The concentration of the water vapor (%) was determined by Eq. (4):

$$c_{\text{H}_2\text{O}} = 10^4 \text{RH} \frac{P_s(T_a)}{P_a} \quad (4)$$

where  $T_a$  (K) represents the gas temperature of the mixing chamber; and  $P_s$  and  $P_a$  represent the saturated vapor pressure (mb) at  $T_a$  and a standard pressure of 1013.25 mb, respectively.

An elemental mercury analyzer (NIC, EMP-2) was used online to detect  $\text{Hg}^0$  at the downstream of the photocatalytic reactor. The decrease in  $\text{Hg}^0$  concentration was mainly attributed to the photo-oxidation of  $\text{Hg}^0$  on the surface of the photocatalysts. The photo-oxidation efficiency ( $\eta$ ) is defined by Eq. (5):

$$\eta(\%) = \frac{\Delta \text{Hg}^0}{\text{Hg}_{\text{in}}^0} = \frac{\text{Hg}_{\text{in}}^0 - \text{Hg}_{\text{out}}^0}{\text{Hg}_{\text{in}}^0} \times 100\% \quad (5)$$

where  $\text{Hg}_{\text{in}}^0$  and  $\text{Hg}_{\text{out}}^0$  represent the concentrations of  $\text{Hg}^0$  at the inlet and outlet of the photocatalytic reactor, respectively. It is noted that the pathway of  $\text{Hg}^0$  could not be distinguished by this measurement system, since  $\text{Hg}^0$  could be either adsorbed onto the surface of the photocatalysts or converted to gaseous oxidized mercury. Therefore, the photo-oxidation efficiency was determined by the difference in the influent and effluent  $\text{Hg}^0$  concentrations. Blank experiments were carried out to validate the mass balance of the experimental setup to exclude errors of concentration resulting from the leakage or adsorption of the glass beads. The blank tests results indicated that  $\text{Hg}^0$  was not adsorbed over the glass beads under near-UV irradiation in  $\text{N}_2$  atmosphere at such a high temperature of 160 °C.

The experimental conditions of the photocatalytic reaction conducted in this study are summarized in Table 1. First, the photo-oxidation efficiencies of  $\text{Hg}^0$  using various photocatalysts were determined at 160 °C in  $\text{N}_2$  atmosphere with influent  $\text{Hg}^0$  concentrations of 25  $\mu\text{g}/\text{m}^3$ . Second, the influence of high temperatures ranging from 120 to 160 °C on the photo-oxidation efficiencies of  $\text{Hg}^0$  by 1–7%  $\text{WO}_3/\text{TiO}_2$  was determined with different influent  $\text{Hg}^0$  concentrations of 25–100  $\mu\text{g}/\text{m}^3$ . In addition, the equilibrium constant ( $K_{\text{Hg}^0}$ ) of  $\text{WO}_3/\text{TiO}_2$  at 120–160 °C was determined by Langmuir-Hinshelwood model. Finally, the effects of single gaseous components on the photo-oxidation efficiency of  $\text{Hg}^0$  were investigated.

## 3. Results and discussion

### 3.1. Characterization of photocatalysts

#### 3.1.1. Specific surface area

The specific surface areas of the  $\text{TiO}_2(\text{Degussa P25})$ ,  $\text{TiO}_2(\text{sol-gel})$  and 1–7%  $\text{WO}_3/\text{TiO}_2$  are summarized in Table 2. The results showed that the BET specific surface areas varied from 43.9  $\text{m}^2/\text{g}$  ( $\text{TiO}_2(\text{Degussa P25})$ ) to 75.1–83.8  $\text{m}^2/\text{g}$  ( $\text{TiO}_2(\text{sol-gel})$  and  $\text{WO}_3/\text{TiO}_2$ ). The BET specific surface area of  $\text{TiO}_2(\text{Degussa P25})$  was lower than that of  $\text{TiO}_2(\text{sol-gel})$  and  $\text{WO}_3/\text{TiO}_2$ , which was consistent with previous studies [18,26]. The larger BET specific surface area of  $\text{WO}_3/\text{TiO}_2$  than that of  $\text{TiO}_2(\text{sol-gel})$  could be attributed to the  $\text{WO}_3$  addition, which inhibited the growth of the anatase when the  $\text{WO}_3/\text{TiO}_2$  was in calcination at 500 °C [19]. Increases in the doping amount of  $\text{WO}_3$  led to a slight increase in specific surface area, from 76.6  $\text{m}^2/\text{g}$  (1%  $\text{WO}_3/\text{TiO}_2$ ) to 83.8  $\text{m}^2/\text{g}$  (7%  $\text{WO}_3/\text{TiO}_2$ ), which was in accordance with a previous report that the specific surface area increased until

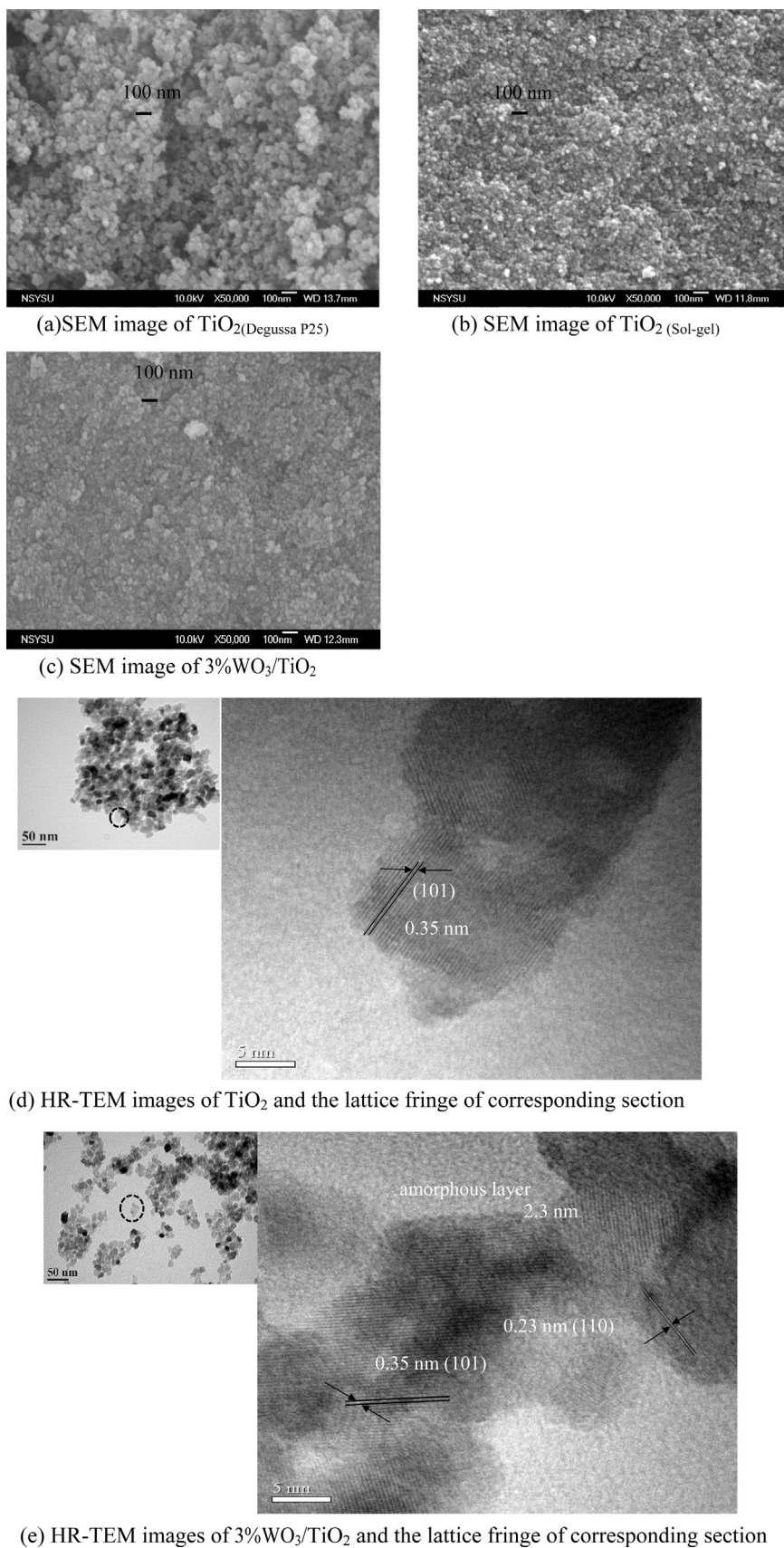


**Fig. 3.** The morphology images of nanoparticles of photocatalysts. ((a)–(c) SEM images of  $\text{TiO}_2$ (DegussaP25),  $\text{TiO}_2$ (sol-gel), and 3%  $\text{WO}_3/\text{TiO}_2$  and (d)–(e) HRTEM images of nanoparticles of  $\text{TiO}_2$ (sol-gel), 3%  $\text{WO}_3/\text{TiO}_2$ ).

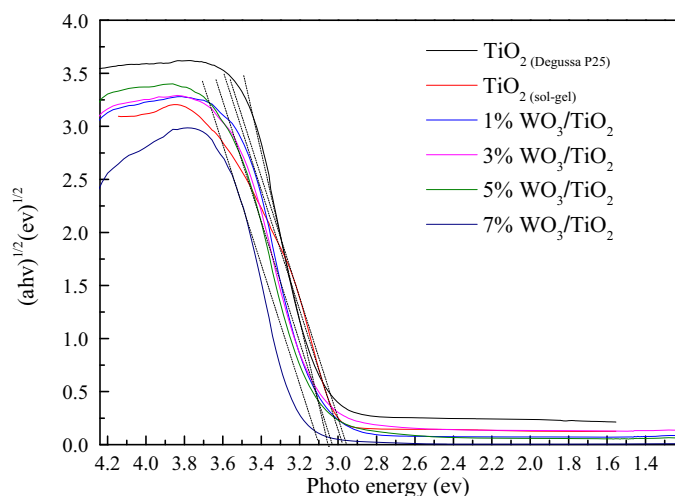


Fig. 4. The UV-vis spectra of  $\text{TiO}_2(\text{Degussa P25})$ ,  $\text{TiO}_2(\text{sol-gel})$ , and 1–7% $\text{WO}_3\text{-TiO}_2$ .

the weight ratio of  $\text{WO}_3$  in  $\text{TiO}_2$  exceeded 20% [19]. The influence of the specific surface area on physical adsorption is significant, and a better physical adsorption capacity is correlated with a higher

specific surface area. However, this study revealed no significant variation between the two preparation methods of the immobilization on the glass beads, because the specific surface area of the photocatalysts was reduced to  $0.015 \text{ m}^2/\text{g}$  ( $\text{TiO}_2(\text{Degussa P25})/\text{glass beads}$ ) and  $0.010 \text{ m}^2/\text{g}$  (1%  $\text{WO}_3/\text{TiO}_2/\text{glass beads}$ ), which was more or less equivalent to the specific surface area of the glass beads. Therefore, the factors influencing the enhancement of  $\text{Hg}^0$  adsorption did not include the variation in specific surface area.

### 3.1.2. Crystallite characterization

Crystallite size, crystallite phase and crystallinity are recognized as important parameters which influence the photocatalytic reactivity of pristine  $\text{TiO}_2$  nanoparticles [33]. The XRD patterns of the photocatalysts are shown in Fig. 2. The crystallite phase of the photocatalysts differed to some extent between  $\text{TiO}_2(\text{sol-gel})$  and Degussa P25, due to the different preparation methods as described above. The crystal patterns, consisting of two phases, anatase and rutile, in  $\text{TiO}_2(\text{Degussa P25})$  (see Table 2), with a mass ratio of 4 (anatase):1 (rutile), were determined by Eq. (2). It is well known that the crystallite formation in Degussa P25 is a physical mixture of anatase (peak at  $25.4^\circ$ ) and rutile (peak at  $27.6^\circ$ ), of which photocatalytic reactivity is superior to either separated anatase or rutile in Degussa P25 [34,35]. In contrast to Degussa

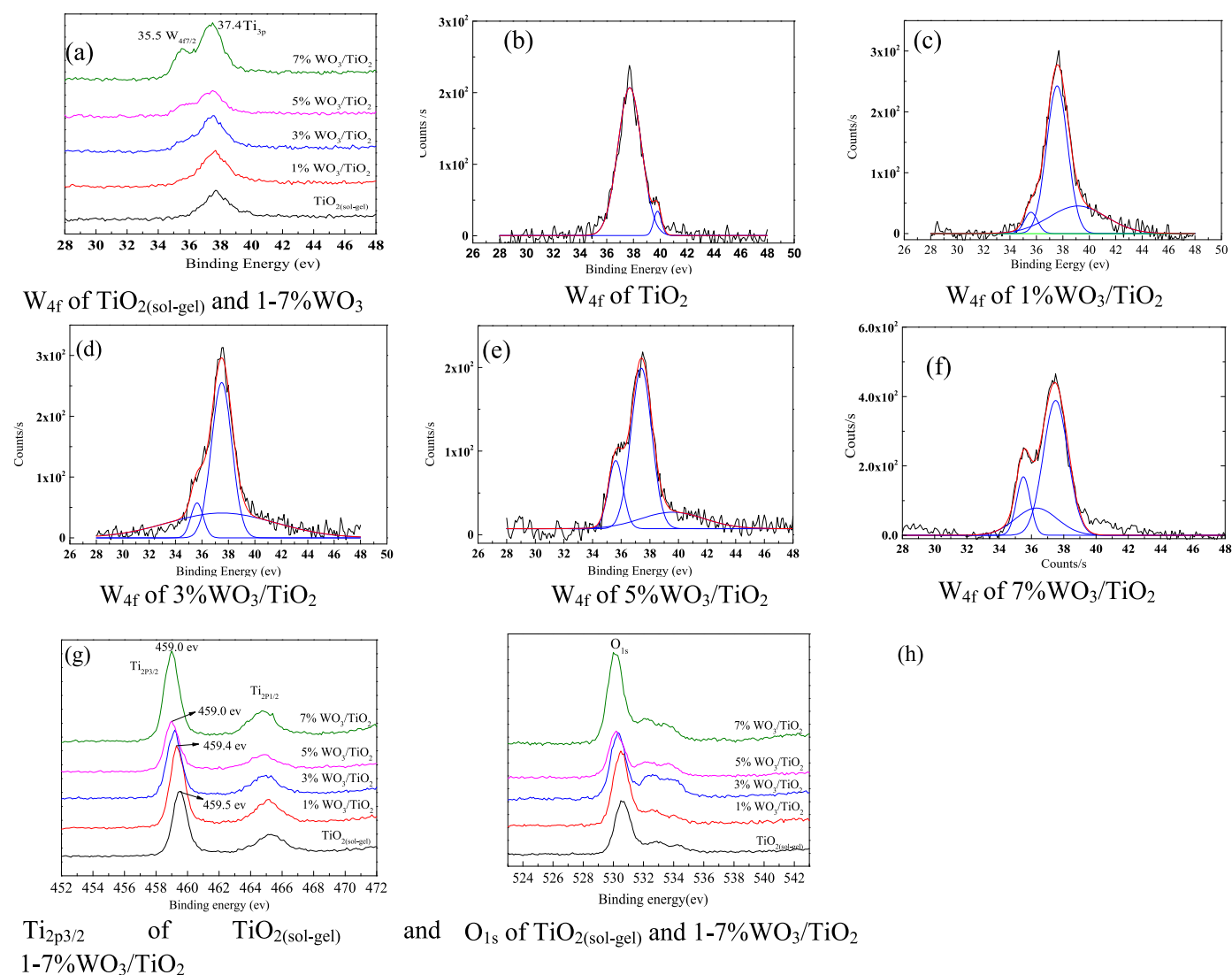


Fig. 5. The XPS spectra of  $\text{TiO}_2(\text{sol-gel})$ , and 1–7% $\text{WO}_3/\text{TiO}_2$ . ((a)–(f)  $\text{W}_{4f}$ ; (g)  $\text{Ti}_{2p}$ ; (h)  $\text{O}_{1s}$ ).

P25, the anatase dominated the crystallite phase, while the rutile phase did not exist in  $\text{TiO}_2(\text{sol-gel})$  or  $\text{WO}_3/\text{TiO}_2$ . In addition, it was observed that the anatase phase was not transformed to the rutile phase for  $\text{TiO}_2(\text{sol-gel})$  or  $\text{WO}_3/\text{TiO}_2$ . It's well known that the optimal reactivity of  $\text{TiO}_2$  in mixed phase of anatase to rutile surpass 90% or less than 30% and the calcination temperature for the phase transformation from anatase to rutile for  $\text{TiO}_2$  is usually at 850 K [36]. The calcination temperature was set as 500 °C lower than 850 K (573 °C) to avoid the growth of rutile crystal and keep the anatase as domination phase.

As determined by the Scherrer equation, the diameters of the anatase and rutile were 22 and 27 nm, respectively, for Degussa P25, while the diameters of the anatase were 13–15 nm for both  $\text{TiO}_2(\text{sol-gel})$  and  $\text{WO}_3/\text{TiO}_2$ . The diameters of  $\text{TiO}_2(\text{sol-gel})$  and  $\text{WO}_3/\text{TiO}_2$  were equivalent, indicating that the addition of tungstate did not change the crystal diameter of  $\text{TiO}_2(\text{sol-gel})$ . According to previous research, the crystal diameters of photocatalysts play a predominant role in influencing their photocatalytic reactivity. Anpo et al. [34] first reported that the reduction of the crystallite size improved the photocatalytic hydrogenation of propyne due to the quantum confinement effect. However, contradictory reports indicated that the increasing of the crystallite size elevated the photocatalytic reactivity due to the optimization of the optical property and charge carrier dynamics [35]. Interestingly, there are also reports suggesting that the optimal crystallite size ranges from 7 to 15 nm for  $\text{TiO}_2$  photocatalytic reactions [37]. Additionally, the peaks of  $23.1^\circ$  (002) and  $33.2^\circ$  (112), both corresponding to  $\text{WO}_3$  crystals [23], did not emerge in the XRD patterns of  $\text{WO}_3/\text{TiO}_2$ , which implied that  $\text{WO}_3$  did not form an independent crystal, but rather either as a highly dispersed amorphous layer of  $\text{WO}_3$  covering the surface of  $\text{TiO}_2$  or incorporation into the titanium lattice by replacing titanium ions with tungsten ions. Previous research has also reported that  $\text{WO}_3$  crystal could be detected by XRD until the loading mass ratio increased up to 40% [38].

The SEM images of the photocatalysts, as illustrated in Fig. 3(a)–(c), showed the  $d_{\text{mean}}$  of the photocatalysts to be in the range of 30 and 50 nm for  $\text{TiO}_2(\text{DegussaP25})$  and 10–20 nm for  $\text{TiO}_2(\text{sol-gel})$  and 3% $\text{WO}_3/\text{TiO}_2$  in accordance with those observed from the XRD patterns, which indicated that the size of the crystallite prepared by sol-gel methods was smaller than that for  $\text{TiO}_2(\text{DegussaP25})$ . From the HRTEM images of  $\text{TiO}_2(\text{sol-gel})$  and 3% $\text{WO}_3/\text{TiO}_2$  as shown in Fig. 3(d) and (e), the crystallite size for 3% $\text{WO}_3/\text{TiO}_2$  ranged from 15 to 20 nm as the same as  $\text{TiO}_2(\text{sol-gel})$ . In addition, the space of lattice fringe of 0.35 nm representing the (101) crystal plane was observed for both  $\text{TiO}_2(\text{sol-gel})$  and 3% $\text{WO}_3/\text{TiO}_2$ , while a different fringe pattern of 0.21–0.23 nm existed in 3% $\text{WO}_3/\text{TiO}_2$  which could be attributed to (110) crystal plane of tungsten oxide [39]. Therefore, a mixture crystal of  $\text{TiO}_2$  and  $\text{WO}_3$  was demonstrated to form in the 3% $\text{WO}_3/\text{TiO}_2$  nanoparticles as shown in Fig. 3(e). On the other hand, a 2.3 nm-thickness prominence observed on the surface of 3% $\text{WO}_3/\text{TiO}_2$  may consist of amorphous  $\text{WO}_3$  [40], which need further verification. These results were in an agreement with the XRD patterns of  $\text{WO}_3/\text{TiO}_2$  which did not show a sole crystal phase of  $\text{WO}_3$  in 1–7% $\text{WO}_3/\text{TiO}_2$ .

### 3.1.3. Light absorption spectrum

The UV–vis spectra of  $\text{TiO}_2(\text{DegussaP25})$ ,  $\text{TiO}_2(\text{sol-gel})$  and  $\text{WO}_3/\text{TiO}_2$  are shown in Fig. 4. A slight variation in the absorption edge of the photocatalysts was observed. The obtained binding gap were 2.99 eV for  $\text{TiO}_2(\text{DegussaP25})$  and 2.96 eV for  $\text{TiO}_2(\text{sol-gel})$ , respectively. Compared with two species of  $\text{TiO}_2$ , the band gap increased from 3.06 eV to 3.20 eV of 1–7% $\text{WO}_3/\text{TiO}_2$  in this study, indicating that the dopant of  $\text{WO}_3$  gradually enlarged the band gap of hybrid structure as the  $\text{WO}_3$  contents increased in the anatase crystal as shown in Fig. 4 and Table 2. It is well known that the tungsten oxide has a broad band gap energy of 2.6–3.3 eV, and the variation of band

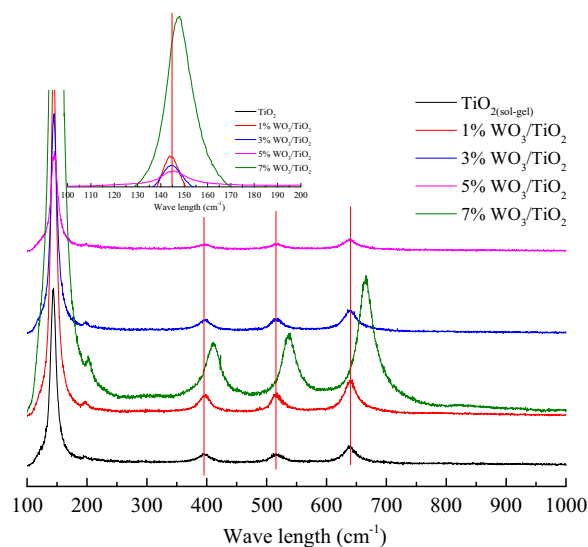


Fig. 6. The Raman spectra of nanoparticles of  $\text{TiO}_2(\text{sol-gel})$ , and 1–7% $\text{WO}_3/\text{TiO}_2$ .

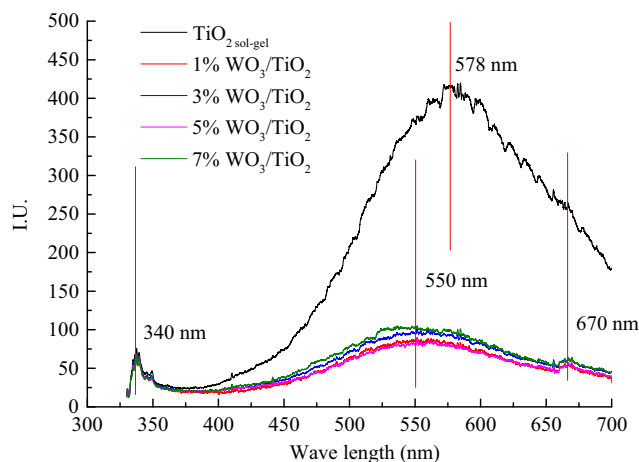


Fig. 7. The photoluminescence (PL) spectra of  $\text{TiO}_2(\text{sol-gel})$  and 1–7% $\text{WO}_3/\text{TiO}_2$ .

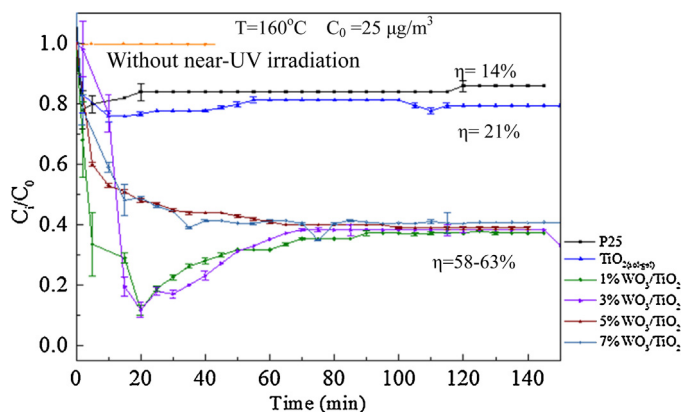


Fig. 8. The photo-oxidation performances of  $\text{TiO}_2$  and  $\text{WO}_3/\text{TiO}_2$  with influent  $\text{Hg}^0$  concentration of  $25 \mu\text{g}/\text{m}^3$  at  $160^\circ\text{C}$  by  $\text{TiO}_2(\text{DegussaP25})$ ,  $\text{TiO}_2(\text{sol-gel})$ , and 1–7% $\text{WO}_3/\text{TiO}_2$  with and without near-UV irradiation.

gap energy depends on preparation methods. He et al. reported that the band gap energy of  $\text{WO}_3/\text{TiO}_2$  prepared using  $\text{Na}_2\text{WO}_4$  and oxalic acid as the precursors was larger than that of  $\text{TiO}_2$  [41]. Additionally, different form of  $\text{WO}_3$  also results in variation of the band gap energy. Higashimoto reported that the band gap of amor-

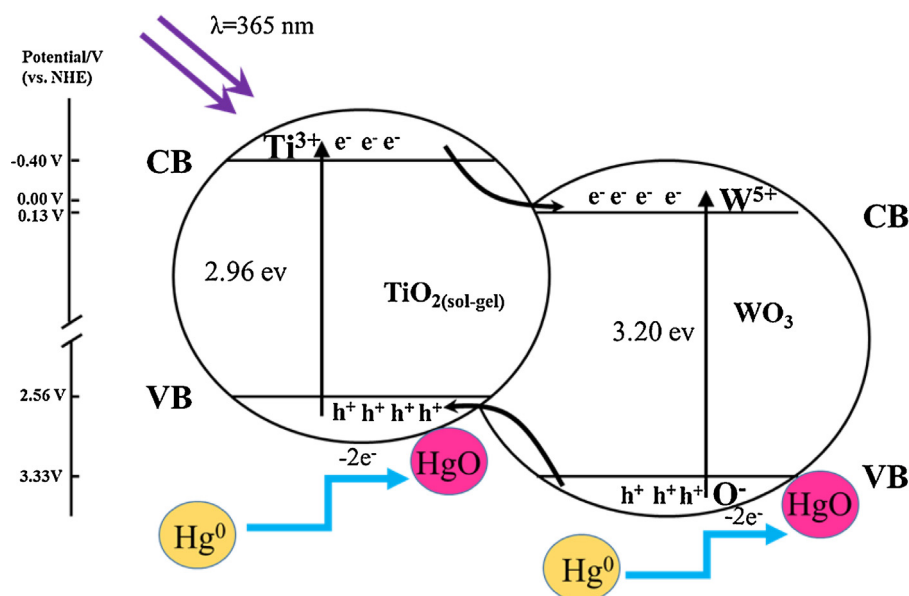


Fig. 9. The schematic diagram of photo-oxidation of  $\text{Hg}^0$  by  $\text{WO}_3/\text{TiO}_2$  under near-UV irradiation.

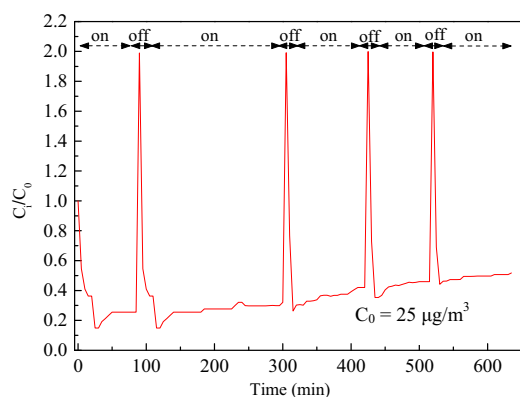


Fig. 10. The stability of photo-oxidation of  $\text{Hg}^0$  by 1%  $\text{WO}_3/\text{TiO}_2$  at 160 °C.

phous  $\text{WO}_3$  (3.4 eV) was larger than that of polycrystalline  $\text{WO}_3$  (2.8 eV) [42]. Since the band gap energy of  $\text{WO}_3/\text{TiO}_2$  composite was larger than that of  $\text{TiO}_2(\text{sol-gel})$ , it was estimated that the band gap of  $\text{WO}_3$  prepared using ammonium tungstate solution could be larger than that of  $\text{TiO}_2(\text{sol-gel})$ , which was possibly attributed to the amorphous phase covering on the surfaces of  $\text{WO}_3/\text{TiO}_2$  or a mixed crystal structure of  $\text{WO}_3$  and  $\text{TiO}_2$ .

Taking the results of band gaps from UV-vis spectra of  $\text{WO}_3/\text{TiO}_2$ , the energy band structure for hybrid  $\text{WO}_3$  coupled with  $\text{TiO}_2$  can be evaluated. It is known that the energy level of the conduction-band minimum ( $E_{\text{CB}}$ ) values of  $\text{WO}_3$  and  $\text{TiO}_2$  are 0.13 and  $-0.40$  V (vs. NHE), respectively. The optical band gaps ( $E_g$ ) of  $\text{WO}_3$  and  $\text{TiO}_2$  were assumed to be 3.20 eV (the real band gap of  $\text{WO}_3$  was higher than 3.20 eV) and 2.96 eV, respectively. Thus, the valence-band maxima (EVB) of  $\text{WO}_3$  and  $\text{TiO}_2$  were 3.33 V and 2.56 V (vs. NHE), respectively.

### 3.1.4. Bond energy

The XPS spectra of the photocatalysts are shown in Fig. 5. The Gaussian equation was used to simulate the peaks of  $\text{W}_{4f7/2}$ , as shown in Fig. 5(a)–(f) and Table S1. The results indicated that a binding energy of 35.6 eV corresponded to the  $\text{W}_{4f7/2}$  energy level. The intensity increased gradually as the  $\text{WO}_3$  doping amount increased on the surface of the  $\text{WO}_3/\text{TiO}_2$ , while the identical peak was not

detected for  $\text{TiO}_2(\text{sol-gel})$  [43] (peak of 37.4 eV corresponded to the  $\text{Ti}_{3p}$  level [44]). Additionally, the chemical states of  $\text{Ti}_{2p3/2}$  and  $\text{O}_{1s}$  varied for  $\text{TiO}_2(\text{sol-gel})$  and  $\text{WO}_3/\text{TiO}_2$ , as shown in Fig. 5(g) and (h). For  $\text{TiO}_2(\text{sol-gel})$ , the binding energy of the  $\text{Ti}_{2p3/2}$  was 490.5 eV attributing to  $\text{Ti}^{4+}$ , while its corresponding energy was 0.5 eV less than  $\text{TiO}_2(\text{sol-gel})$  for  $\text{WO}_3/\text{TiO}_2$ . The  $\text{O}_{1s}$  of 530.5 eV and 532.9 eV may have originated from the crystal of the O atom and the hydroxyl adsorbed on the  $\text{TiO}_2(\text{sol-gel})$  surface [28,45], respectively, while the corresponding binding energies of 530.1 eV and 532.0 eV were present in the  $\text{WO}_3/\text{TiO}_2$ . The gradual shift towards a lower energy level indicating that the binding energy of  $\text{Ti}_{2p3/2}$  and  $\text{O}_{1s}$  changed as the loading of  $\text{WO}_3$  interfered with the energy level of  $\text{TiO}_2$ , which may originate from the mixed crystal structure between  $\text{TiO}_2$  and  $\text{WO}_3$ . Otherwise, the binding energy of  $\text{Ti}_{2p3/2}$  would not vary when the modification of  $\text{WO}_3$  was conducted by doping the tungstate precursor into Degussa P25 [43].

### 3.1.5. Raman spectra

The Raman spectra of  $\text{TiO}_2(\text{sol-gel})$  and  $\text{WO}_3/\text{TiO}_2$  are illustrated in Fig. 6. The peaks were present at about 144 ( $E_g$ ), 197 ( $B_{1g}$ ), 515 ( $B_{2g}$ ) and 640 ( $E_g$ )  $\text{cm}^{-1}$ , corresponding to the typical vibration modes of anatase for  $\text{TiO}_2(\text{sol-gel})$ . Two different Raman patterns occurred in  $\text{WO}_3/\text{TiO}_2$ , indicating that different structures resulted from different  $\text{WO}_3$  loadings. The patterns of 1–5%  $\text{WO}_3/\text{TiO}_2$  were similar to those of  $\text{TiO}_2(\text{sol-gel})$ , indicating that no new modes were detected for the lower loading amount of  $\text{WO}_3$ . Due to a blue-shift and broadening, the corresponding peaks of the anatase modes were present at 148, 203, 413, 537 and 665  $\text{cm}^{-1}$  for 7%  $\text{WO}_3/\text{TiO}_2$ , respectively. This phenomenon was in agreement with a previous study [46]. The variation in the vibration mode for 7%  $\text{WO}_3/\text{TiO}_2$  could be explained by the appearance of tensile stress at the interface of  $\text{WO}_3$  and  $\text{TiO}_2$  [46].

### 3.1.6. Fluorescence emission spectra

The photoluminescence (PL) emission spectra resulting from the recombination of photo-induced electrons and photons can be assigned to the radiative recombination of self-trapped excitons and impurity-trapped excitons [47]. The PL emission spectra of  $\text{TiO}_2(\text{sol-gel})$  and  $\text{WO}_3/\text{TiO}_2$  showed that the intensity and location of peaks differed between  $\text{TiO}_2(\text{sol-gel})$  and  $\text{WO}_3/\text{TiO}_2$ , as shown in Fig. 7. For  $\text{TiO}_2(\text{sol-gel})$ , the luminance emission of 575 nm in this

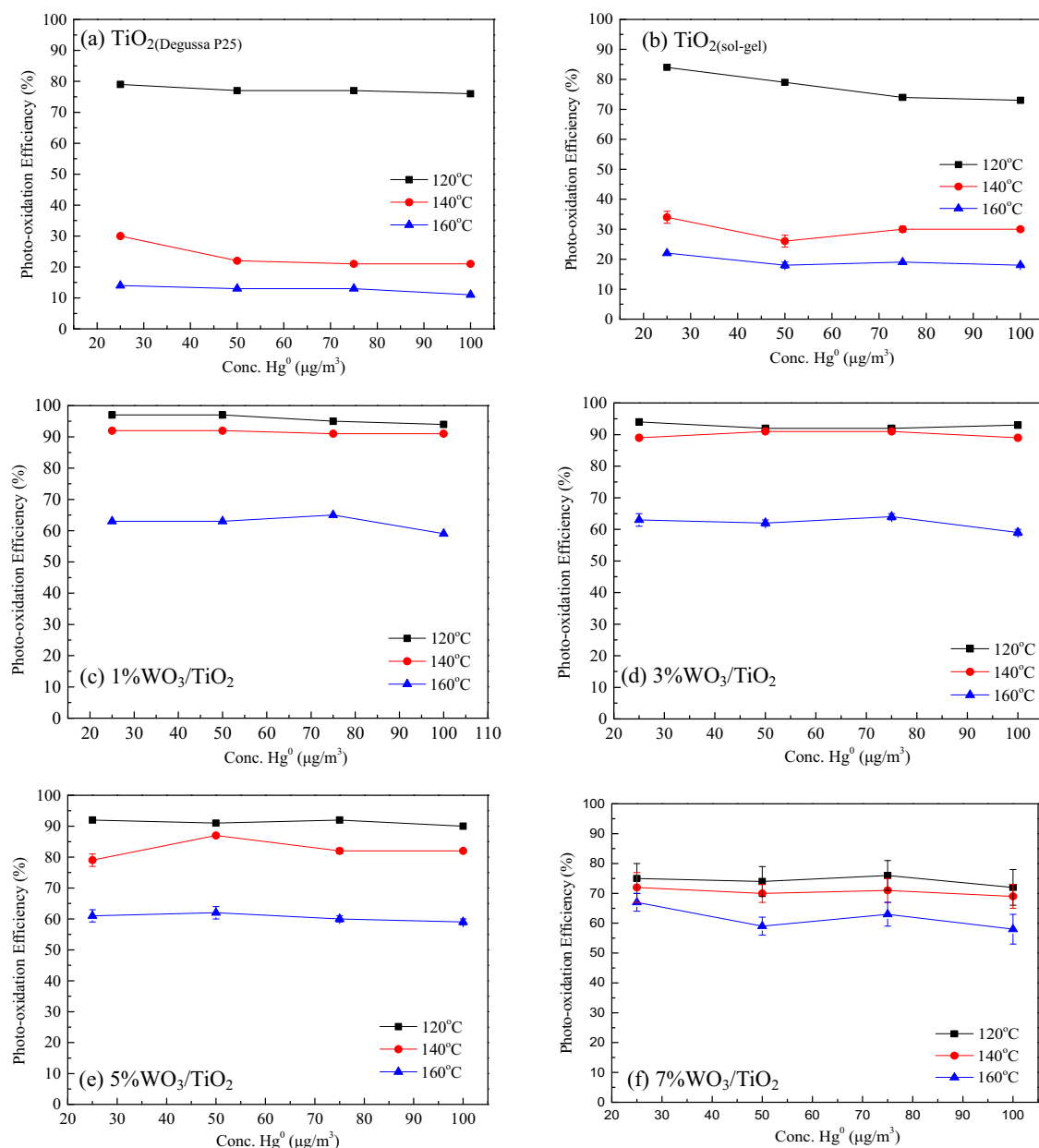


**Fig. 11.** The photo-oxidation efficiencies of Hg<sup>0</sup> with different initial concentrations of 25–100 μg/m<sup>3</sup> Hg<sup>0</sup> at 120–160 °C by TiO<sub>2</sub>(DegussaP25), TiO<sub>2</sub>, 1–7% WO<sub>3</sub>/TiO<sub>2</sub> ((a) TiO<sub>2</sub>(DegussaP25), (b) TiO<sub>2</sub>(sol-gel), (c)–(f) 1–7% WO<sub>3</sub>/TiO<sub>2</sub>).

study (longer than the 500 nm in a previous study [48], possibly due to the lattice deformation) was attributed to the charge-transfer transition from Ti<sup>3+</sup> to an oxygen atom. As compared to TiO<sub>2</sub>(sol-gel), the main peak shifted toward a shorter wavelength of 550 nm in WO<sub>3</sub>/TiO<sub>2</sub>. Since the PL wavelength is related closely to the energy position of the triplet state relative to the ground state, the position shift of the main peak towards a shorter wavelength elucidates that the energy gap between the lowest triplet state and the ground singlet state becomes enlarged [49]. Doping WO<sub>3</sub> into the TiO<sub>2</sub> lattice created a larger band gap and consequently resulted in a blue shift for WO<sub>3</sub>/TiO<sub>2</sub> compared with that of TiO<sub>2</sub>(sol-gel). In addition, the main PL emission intensity of WO<sub>3</sub>/TiO<sub>2</sub> was rather lower than that of TiO<sub>2</sub>(sol-gel), indicating that the recombination rate of photo-induced electrons and holes had decreased. Consequently, the photo-induced electrons and holes were efficiently separated [45]. The separation can be obtained from the band gap structure of WO<sub>3</sub>/TiO<sub>2</sub> and was resulted from that the photo-induced electrons

were transferred from a conduction band of TiO<sub>2</sub> to a conduction band of WO<sub>3</sub>, and the holes accumulated in a valence band of TiO<sub>2</sub> from a valence band of WO<sub>3</sub>.

### 3.2. Photo-oxidation efficiency of Hg<sup>0</sup> for various photocatalysts

#### 3.2.1. Effects of reaction temperature on photo-oxidation efficiency of Hg<sup>0</sup>

Fig. 8 illustrates the photo-oxidation efficiencies of Hg<sup>0</sup> at 160 °C by TiO<sub>2</sub>(DegussaP25), TiO<sub>2</sub>(sol-gel) and 1–7% WO<sub>3</sub>/TiO<sub>2</sub> with an influent Hg<sup>0</sup> concentration of 25 μg/m<sup>3</sup>. A blank test without near-UV irradiation was conducted prior to each photo-oxidation test for different photocatalysts. The results showed that without near-UV irradiation, the removal efficiency of Hg<sup>0</sup> was null (0%) for each photocatalyst at 160 °C as shown in Fig. 8. Hg<sup>0</sup> was not adsorbed over the surfaces of TiO<sub>2</sub> and WO<sub>3</sub>/TiO<sub>2</sub> at such a high temperature without near-UV irradiation, while once the near-UV irradiation

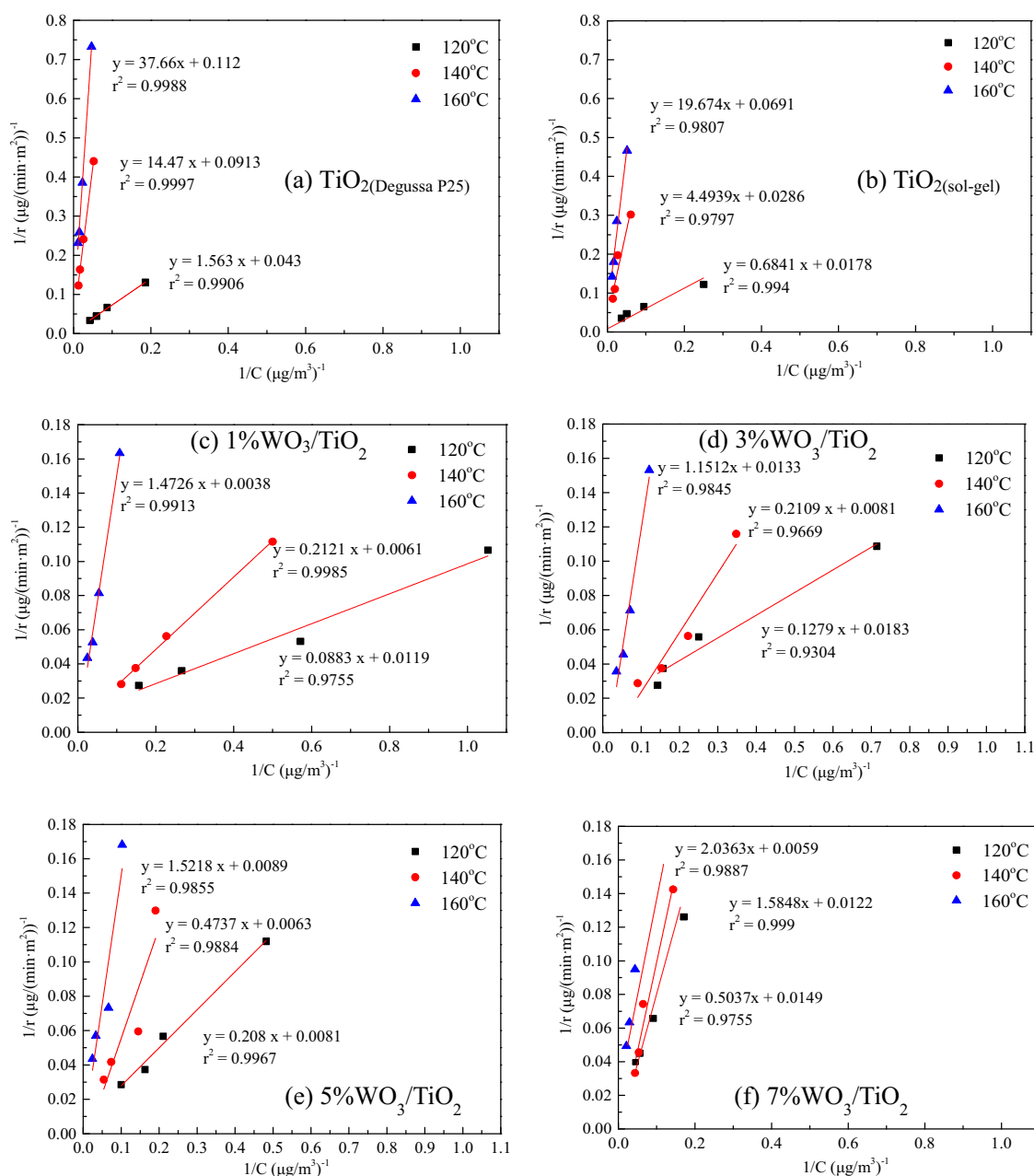


**Fig. 12.** The Langmuir-Hinshelwood model for  $\text{TiO}_2(\text{DegussaP25})$ ,  $\text{TiO}_2(\text{sol-gel})$  and 1–7%  $\text{WO}_3/\text{TiO}_2$  to determine the  $K_{\text{Hg}^0}$  of the photo-oxidation reactions. ((a)  $\text{TiO}_2(\text{DegussaP25})$ ), (b)  $\text{TiO}_2(\text{sol-gel})$ , (c)–(f) 1–7%  $\text{WO}_3/\text{TiO}_2$ ).

was introduced to the  $\text{Hg}^0$  removal system, the effluent  $\text{Hg}^0$  concentration immediately began to drop. It can be inferred that the removal mechanism can not be attributed to thermo-catalytic oxidation by  $\text{TiO}_2$  and  $\text{WO}_3/\text{TiO}_2$  but rather a photocatalytic oxidation. The results shown in Fig. 8 also indicate a photo-oxidation efficiency of  $\text{Hg}^0$  by various photocatalysts in a descending order of  $\eta(\text{WO}_3/\text{TiO}_2) > \eta(\text{TiO}_2(\text{sol-gel})) > \eta(\text{TiO}_2(\text{DegussaP25}))$ .

It is well known that, at ambient temperature,  $\text{TiO}_2(\text{DegussaP25})$  can nearly reach a high efficiency of above 90% [50–52], while above 120 °C, the gradually increasing temperature inhibits the photocatalytic reactivity of  $\text{TiO}_2(\text{DegussaP25})$  and reduces the photo-oxidation efficiency of  $\text{Hg}^0$ . As shown in Fig. S2, the photo-oxidation efficiency of  $\text{Hg}^0$  improved slightly from 25% ( $\text{TiO}_2(\text{DegussaP25})$ ) to 40% ( $\text{TiO}_2(\text{sol-gel})$ ) at 140 °C and from 14% ( $\text{TiO}_2(\text{DegussaP25})$ ) to 21% ( $\text{TiO}_2(\text{sol-gel})$ ) at 160 °C, respectively. The enhancement was mainly attributed to there being more anatase and smaller crystal sizes for

$\text{TiO}_2(\text{sol-gel})$ , as compared to  $\text{TiO}_2(\text{DegussaP25})$ , based on the characterization analysis. It is generally considered that a wider band gap of anatase generates a higher electrical potential than rutile, and that the improved electrical conductivity as a result of smaller diameters separates the photo-induced holes and electrons effectively [11].

As compared to  $\text{TiO}_2(\text{sol-gel})$ , 1–7%  $\text{WO}_3/\text{TiO}_2$  enhanced the photo-oxidation efficiencies of  $\text{Hg}^0$  by more than 60%, as shown in Fig. 8. Based on the photocatalysts' characterization results, there was no significant variation in specific surface area, the crystal size or crystal structure between  $\text{WO}_3/\text{TiO}_2$  and  $\text{TiO}_2(\text{sol-gel})$ . Accordingly, the promotion of the photo-oxidation efficiency of  $\text{Hg}^0$  by  $\text{WO}_3/\text{TiO}_2$  was mainly attributed to the successful doping of  $\text{WO}_3$  onto the surface of  $\text{TiO}_2$ , which changed its surface chemical composition. The possible activated sites for  $\text{Hg}^0$  adsorption on the surface of  $\text{WO}_3/\text{TiO}_2$  were considered to be the oxygen atom of crys-

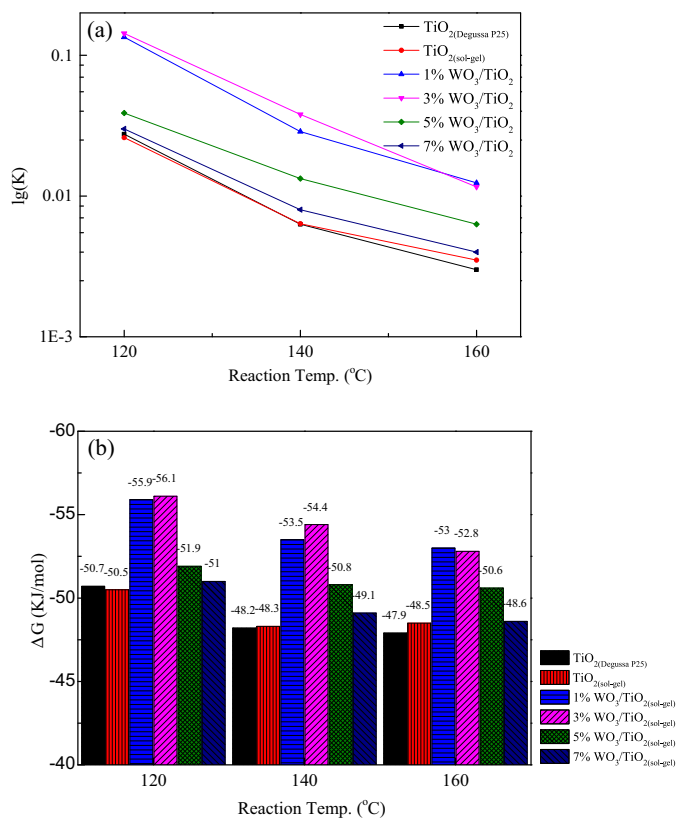


Fig. 13. The determined equilibrium constants  $K_{Hg0}$  and  $\Delta G$  for  $TiO_2$ (Degussa P25),  $TiO_2$ (sol-gel) and 1–7% $WO_3/TiO_2$ . ((a)  $K_{Hg0}$ , (b)  $\Delta G$ ).

tal of  $WO_3$ ,  $TiO_2$  and the bridge one located between the titanium (Ti) and the tungsten (W) atom. The mechanism consisted of several steps as shown in Fig. 9 and chemical Eqs. (6)–(9): (1) the photo-induced electrons were transferred from the oxygen of  $WO_3$ ,  $TiO_2$ , and the bridge oxygen, to  $Ti^{4+}$  or  $W^{6+}$  under the near-UV irradiation, which initiated the oxygen into a excited state with capability of accepting electrons from  $Hg^0$ . (2) When  $Hg^0$  was adsorbed on the oxygen atom, its outer electrons were readily to be neutralized by the photo-induced hole of excited oxygen atom. (3)  $Hg^0$  was oxidized to  $HgO$  by the oxygen and then fixed on the surface of the  $TiO_2$  and  $WO_3/TiO_2$ . It's worth noting that the oxidized  $HgO$  has not been detected from the effluent stream in our recent investigation, which illustrated that the Hg was strongly adsorbed on the surface of  $WO_3/TiO_2$ . Therefore, at such high temperatures, the removal of  $Hg^0$  can not be attributed to the physical adsorption but most likely the chemisorption.

In addition, the photo-oxidation was enhanced by the conjunction of  $WO_3$  and  $TiO_2$ , because the photo-induced electrons and holes were efficiently separated in the way that the photo-induced electrons of  $TiO_2$  easily moved towards the conduction band of  $WO_3$  while the photo-induced holes of  $WO_3$  moved towards the valance band of  $TiO_2$ .



To test the stability of the photocatalysts, the photo-oxidation of  $Hg^0$  by 1% $WO_3/TiO_2$  was performed within 600 min for 5 on-off turns with influent  $Hg^0$  concentration of 25  $\mu g/m^3$  as shown in Fig. 10. The results illustrated that the photo-oxidation efficiency

of  $Hg^0$  decreased <10% within 600 min. It's noted that although the  $WO_3$  dopant improved the photocatalytic reactivity  $TiO_2$  for  $Hg^0$  removal, the photo-oxidation efficiency decreased gradually as the activated sites of  $WO_3/TiO_2$  were occupied by  $Hg^0$  in the atmosphere of  $N_2$ .

The influence of high temperature on the photo-oxidation reaction of  $Hg^0$  can be described by Eq. (10):

$$K_{Hg0} = \frac{C_{TiO_2-Hg}}{C_{Hg0}} = K' \frac{\exp\left(-\frac{\Delta H}{RT}\right)}{\sqrt{T}} \quad (10)$$

where  $C_{TiO_2-Hg}$  is the concentration of the adsorbed  $Hg^0$ ;  $C_{Hg0}$  is the gaseous  $Hg^0$  concentration;  $K'$  is the unvaried equilibrium constant;  $\Delta H$  (J/mol) is the change of enthalpy for the photo-oxidation reaction between  $Hg^0$  and  $TiO_2$ ; and  $T$ (K) is the reaction temperature. The photo-oxidation reaction is an exothermic process and, thus,  $K_{Hg0}$  decreased when the reaction temperature ( $T$ ) increased [9,53]. According to Eq. (10), we inferred that the effect of  $WO_3$  doping increased the reaction entropy ( $\Delta H$ ) between  $WO_3/TiO_2$  and  $Hg^0$  which was larger than that between  $TiO_2$  and  $Hg^0$ ; hence, the adverse effects resulting from the increased reaction temperature were diminished by doping  $WO_3$ .

### 3.2.2. Effects of $WO_3$ doping on the photo-oxidation efficiency of $Hg^0$

The effects of the amount of  $WO_3$  doping on the photo-oxidation efficiencies at 120–160 °C were also investigated with different influent  $Hg^0$  concentrations. As shown in Fig. 11, when the reaction temperature was upped to 140 °C, doping  $WO_3$  promoted the photo-oxidation efficiencies of  $Hg^0$  to higher than 80% for 1, 3 and 5%  $WO_3/TiO_2$  and to about 70% for 7%  $WO_3/TiO_2$ , while the efficiencies were higher than 60% for 1–7%  $WO_3/TiO_2$  at 160 °C, 2–4 times higher than those of  $TiO_2$ (DegussaP25) and  $TiO_2$ (sol-gel). The results of the varied photo-oxidation efficiencies with different  $WO_3$  doping amounts showed that 3 and 5%  $WO_3/TiO_2$  performed better than 1% and 7%  $WO_3/TiO_2$  at 160 °C, and that 1, 3 and 5%  $WO_3/TiO_2$  were better than 7%  $WO_3/TiO_2$  at 140 °C.

The equilibrium constant ( $K_{Hg0}$ ) was also determined by the Langmuir-Hinshelwood model in order to investigate the effect of the  $WO_3$  doping amount [54–56]. The detailed description for determining the  $K_{Hg0}$  can be referenced in previous research [57]; the equation is:

$$r = \frac{(C_{Hg0in} - C_{Hg0out}) \times Q}{A} \quad (11)$$

where  $C_{Hg0in}$  ( $\mu g m^{-3}$ ) is the influent  $Hg^0$  concentration of the reaction system;  $C_{Hg0out}$  ( $\mu g m^{-3}$ ) is the effluent  $Hg^0$  concentration of the reaction system at steady state;  $Q$  (mL/min) is the overall flow rate (mL min<sup>-1</sup>); and  $A$  is the total surface area of the glass beads in the reactor and equal to 21.8 cm<sup>2</sup> through determination. The L-H model can be described by Eq. (12):

$$r = k \frac{K_{Hg0} C_{Hg0}}{1 + K_{Hg0} C_{Hg0}} \quad (12)$$

where  $r$  is the photo-oxidation rate of  $Hg^0$  ( $\mu g m^{-2} min^{-1}$ );  $k$  is the photo-oxidation rate constant ( $\mu g m^{-2} min^{-1}$ );  $K_{Hg0}$  is the equilibrium constant of  $Hg^0$  ( $m^3 \mu g^{-1}$ ); and  $C_{Hg0}$  is the outlet concentration of  $Hg^0$  at steady state. The inverse of Eq. (12) can be expressed as:

$$\frac{1}{r} = \frac{1}{k K_{Hg0}} \frac{1}{C_{Hg0}} + \frac{1}{k} \quad (13)$$

If the L-H expression is valid for  $Hg^0$  photocatalytic oxidation, a plot of  $r^{-1}$  vs  $C_{Hg0}^{-1}$  should be linear [57]. Subsequently, the values of  $K_{Hg0}$  can be obtained by dividing the intercept by the slope of the linear line. The Langmuir-Hinshelwood models for  $TiO_2$ (DegussaP25),

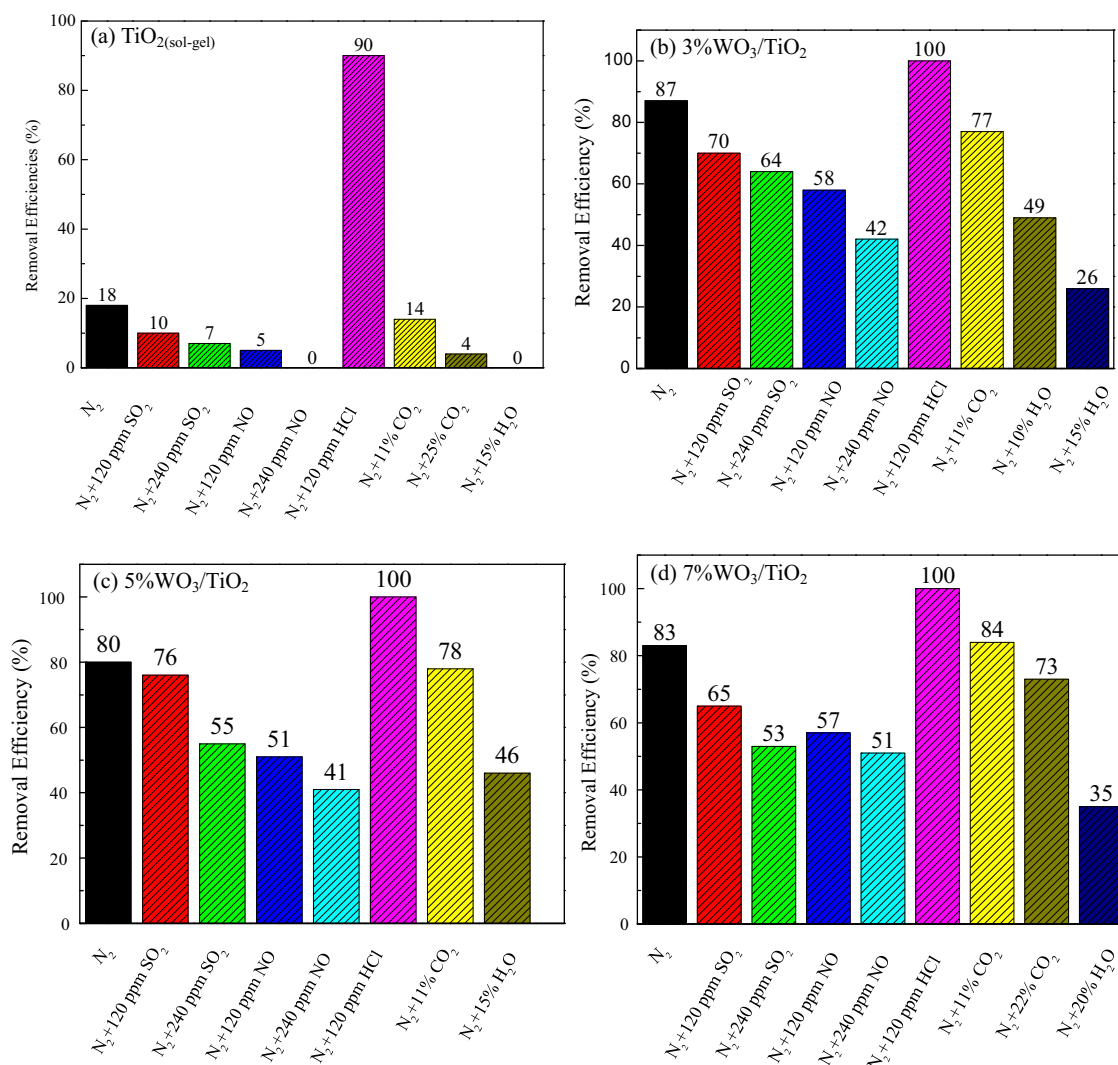


**Fig. 14.** The effect of single gas component on the photo-oxidation efficiency of Hg<sup>0</sup> at 160 °C by TiO<sub>2</sub>(sol-gel), 1–5%WO<sub>3</sub>/TiO<sub>2</sub>. ((a) TiO<sub>2</sub>(sol-gel), (b) 3%WO<sub>3</sub>/TiO<sub>2</sub>, (c) 5%WO<sub>3</sub>/TiO<sub>2</sub>, (d) 7%WO<sub>3</sub>/TiO<sub>2</sub>).

TiO<sub>2</sub>(sol-gel) and 1–7% WO<sub>3</sub>/TiO<sub>2</sub> are described in Fig. 12. The results showed that most of the regression coefficients at different temperatures were above 0.98, suggesting that the L-H model fit the photo-oxidation of Hg<sup>0</sup> quite well. The  $k$  was not discussed in this study, since it is usually used to evaluate the time needed for a reaction to reach the steady state. The photo-oxidation of Hg<sup>0</sup> by the photocatalysts reached steady state after 10–40 min, as shown in Figs. 8 and S2.  $K_{\text{Hg}^0}$  was investigated carefully because of its close correlation to the  $\Delta G$  released from the photo-oxidation of Hg<sup>0</sup> on the surfaces of photocatalysts. The  $K_{\text{Hg}^0}$  for the catalysts at different temperatures is shown in Fig. 13(a).  $K_{\text{Hg}^0}$  decreased as the reaction temperatures increased, showing a similar trend as the photo-oxidation efficiencies, illustrating that higher temperatures could decrease the adsorption equilibrium between Hg<sup>0</sup> and the surfaces of TiO<sub>2</sub>(DegussaP25), TiO<sub>2</sub>(sol-gel) and WO<sub>3</sub>/TiO<sub>2</sub>.

The  $K_{\text{Hg}^0}$  of TiO<sub>2</sub>(DegussaP25), TiO<sub>2</sub>(sol-gel) and WO<sub>3</sub>/TiO<sub>2</sub> varied significantly, and  $K_{\text{Hg}^0}$  was much smaller for TiO<sub>2</sub>(DegussaP25) and TiO<sub>2</sub>(sol-gel) than for WO<sub>3</sub>/TiO<sub>2</sub>, which illustrated that the addition of WO<sub>3</sub> was of real benefit for the photo-oxidation of Hg<sup>0</sup>. In addition, different doping amounts of WO<sub>3</sub> also led to different  $K_{\text{Hg}^0}$  values for 1–7% WO<sub>3</sub>/TiO<sub>2</sub>. At 120 and 140 °C,  $K_{\text{Hg}^0}$  was higher for 1 and 3% WO<sub>3</sub>/TiO<sub>2</sub> than for 5 and 7% WO<sub>3</sub>/TiO<sub>2</sub>; conversely, the  $K_{\text{Hg}^0}$  for 7% WO<sub>3</sub>/TiO<sub>2</sub> was a little higher than 1 and 3% WO<sub>3</sub>/TiO<sub>2</sub> at 160 °C,

which was in agreement with the variation in the photo-oxidation efficiencies of Hg<sup>0</sup> for WO<sub>3</sub>/TiO<sub>2</sub>. This meant that the continuous increase in the WO<sub>3</sub> doping amount decreased the  $K_{\text{Hg}^0}$  and photo-oxidation efficiencies for WO<sub>3</sub>/TiO<sub>2</sub>, possibly because of the steric effect on the adsorption of Hg<sup>0</sup> as the result of higher amounts of WO<sub>3</sub> on the surfaces [58].

In addition, the  $\Delta G$  of a chemical reaction can be determined by Eq. (14),

$$\Delta G = -\ln(K)RT \quad (14)$$

where  $R$  is the ideal gas constant, 8.314 J/molK. The  $\Delta G$  of each photocatalytic reaction ranged from  $-50.7$  to  $-47.9$  kJ/mol for TiO<sub>2</sub>(DegussaP25) and from  $-50.5$  to  $-48.3$  kJ/mol for TiO<sub>2</sub>(sol-gel), as shown in Fig. 13(b). As compared to TiO<sub>2</sub>(DegussaP25) and TiO<sub>2</sub>(sol-gel),  $\Delta G$  showed an obvious increase for 1, 3 and 5% WO<sub>3</sub>/TiO<sub>2</sub> to higher than 50 kJ/mol. For example, at 160 °C, the energy of  $-47.9$  kJ/mol for TiO<sub>2</sub>(DegussaP25) increased to  $-48.5$  kJ/mol for TiO<sub>2</sub>(sol-gel), and even to  $-53$  kJ/mol for 1% WO<sub>3</sub>/TiO<sub>2</sub>. It is worth noting that the change of  $\Delta G$  was equal to  $\Delta H - T\Delta S$ , and that  $\Delta H$  and  $\Delta S$  varied with the reaction temperature, making it hard to estimate their values at different temperatures. Therefore,  $\Delta H$  and  $\Delta S$  were not discussed in this study.

### 3.2.3. Effects of single gas component on Hg<sup>0</sup> photo-oxidation efficiency

The effects of a single gas component on the photo-oxidation efficiency of Hg<sup>0</sup> by TiO<sub>2</sub>(sol-gel) and 1–5% WO<sub>3</sub>/TiO<sub>2</sub> are shown in Fig. 14. The existence of SO<sub>2</sub> (120 ppm or 240 ppm) inhibited the photo-oxidation of Hg<sup>0</sup>, because its concentration was one thousand times higher than the Hg<sup>0</sup> concentration and a competitive adsorption occurred on the surface of TiO<sub>2</sub>(sol-gel) and WO<sub>3</sub>/TiO<sub>2</sub> between SO<sub>2</sub> and Hg<sup>0</sup>. The phenomenon of a high effluent concentration of Hg<sup>0</sup> being immediately released after SO<sub>2</sub> was added into the photo-oxidation system (not shown in this article) implied that SO<sub>2</sub> could replace the adsorbed Hg and then occupy the active sites on the TiO<sub>2</sub>(sol-gel) and WO<sub>3</sub>/TiO<sub>2</sub> surfaces. Finally, an equilibrium reached toward a lower photo-oxidation efficiency of Hg<sup>0</sup>; we inferred the inhibition resulted from the depletion of the available active sites of WO<sub>3</sub> for Hg<sup>0</sup> adsorption by SO<sub>2</sub>. Previous researches have reported a contrary phenomenon, i.e., that at 20–135 °C, the effect of SO<sub>2</sub> was positive or without side effects on the reactivity of TiO<sub>2</sub> [59], suggesting that there was no interaction between SO<sub>2</sub> molecules and TiO<sub>2</sub>.

The NO had an adverse effect on the photo-oxidation efficiency of Hg<sup>0</sup> by TiO<sub>2</sub>(sol-gel) and WO<sub>3</sub>/TiO<sub>2</sub>, as seen in Fig. 14. The reason could be that the adsorption of NO occurred on the surface of TiO<sub>2</sub>(sol-gel) and WO<sub>3</sub>/TiO<sub>2</sub> because the OH radicals on TiO<sub>2</sub> were scavenged by NO [59] or WO<sub>3</sub> as Lewis acid had acquired electrons from NO [60,61] during the Hg<sup>0</sup> photo-oxidation.

The effect of H<sub>2</sub>O was the inhibition of the photo-oxidation efficiency of Hg<sup>0</sup>, which was in an agreement with previous research [62]. The photo-oxidation efficiency of Hg<sup>0</sup> decreased from 80% to 20–50% when 4700–5900 ppmv H<sub>2</sub>O was added into the system, indicating that water vapor molecules competed with Hg<sup>0</sup> molecules for the available active sites. When humid air passed through the reactor, the superhydrophilic surface of TiO<sub>2</sub> attracted excessive amounts of water, resulting in the ejection of adsorbed Hg<sup>0</sup> from the surface [62], as expressed in Eq. (15):



However, HCl was beneficial in enhancing the oxidation of Hg<sup>0</sup> by TiO<sub>2</sub>-based photocatalysts [63,64]. The photo-oxidation efficiency of Hg<sup>0</sup> reached 90% for TiO<sub>2</sub>(sol-gel) and 100% for WO<sub>3</sub>/TiO<sub>2</sub> with the existence of 120 ppm HCl. When the irradiation of UV light was turned off but in the atmosphere of HCl, the removal efficiency of Hg<sup>0</sup> still remained about 50%, which implied that HCl could be strongly adsorbed on the surface of TiO<sub>2</sub>(sol-gel) and WO<sub>3</sub>/TiO<sub>2</sub>, resulting in a prolonged and relatively high photo-oxidation efficiency of Hg<sup>0</sup> even without irradiation. This promotion by HCl fit well with the Langmuir-Hinshelwood model [63].

As compared with other acidic gases, the effect of a high concentration of CO<sub>2</sub> (12–22%v/v) on the photo-oxidation of Hg<sup>0</sup> was negligible.

## 4. Conclusions

The photo-oxidation of Hg<sup>0</sup> at high temperatures of 120–160 °C was conducted using TiO<sub>2</sub>(DegussaP25), TiO<sub>2</sub>(sol-gel) and 1–7% WO<sub>3</sub>/TiO<sub>2</sub> as photo-catalysts. The photo-catalysts were successfully coated onto the surfaces of glass beads. The photo-oxidation efficiency of Hg<sup>0</sup> was greatly enhanced by WO<sub>3</sub> dopant at a high temperature of 160 °C (from 14% for P25 to 63% for WO<sub>3</sub>/TiO<sub>2</sub>). The improvement was due to the modification of WO<sub>3</sub> that enlarged the band gap energy of TiO<sub>2</sub> and effectively promoted the separation of photo-induced electrons and holes. The different WO<sub>3</sub> doping amounts also affected the photo-oxidation efficiency of Hg<sup>0</sup>, and the photocatalytic reactivity of 1–3% WO<sub>3</sub>/TiO<sub>2</sub> was superior to that of 5–7% WO<sub>3</sub>/TiO<sub>2</sub>. The equilibrium of K<sub>Hg0</sub> and Gibbs

free energy of ΔG were determined by the L-H model simulation. Higher temperatures above 140 °C decreased the K<sub>Hg0</sub> and ΔG of the photo-oxidation. The effect of a single gas component on the photo-oxidation of Hg<sup>0</sup> illustrated that HCl enhanced, while NO, SO<sub>2</sub> and H<sub>2</sub>O reduced, the photo-oxidation efficiencies of Hg<sup>0</sup> by TiO<sub>2</sub>(sol-gel) and WO<sub>3</sub>/TiO<sub>2</sub>.

## Acknowledgements

This study was performed under the auspices of Ministry of Science and Technology (MOST), Republic of China, under the contract number 101-2221-E-110-058-MY3. The authors are grateful to the Ministry of Science and Technology for its financial support.

## Appendix A. Supplementary data

Supplementary data associated with this article can be found, in the online version, at <http://dx.doi.org/10.1016/j.apcatb.2016.04.045>.

## References

- [1] E.G. Pacyna, J.M. Pacyna, *At. Environ.* 35 (2001) 2987–2996.
- [2] M. Sakata, K. Marumoto, *Atmos. Environ.* 36 (2002) 239–246.
- [3] J.H. Pavlish, A.E. Sondreal, D.M. Mann, S.E. Olson, C.K. Galbreath, L.D. Laudal, A.S. Benson, *Fuel Process. Technol.* 82 (2003) 89–165.
- [4] [www.mercuryconvention.org/Convention/tabid/3426/Default.aspx](http://www.mercuryconvention.org/Convention/tabid/3426/Default.aspx).
- [5] U. Kaluza, H.P. Boehm, *J. Catal.* 22 (1971) 347–358.
- [6] C.Y. Wu, T.G. Lee, G. Tyree, E. Arar, P. Biswas, *Environ. Eng. Sci.* 2 (1998) 137–148.
- [7] D. Pudasainee, J.H. Kim, Y.S. Yoon, Y.C. Seo, *Fuel* 93 (2012) 312–318.
- [8] J.F. Wu, C.H. Hung, C.S. Yuan, *Photochem. Photobiol. A Chem.* 170 (2005) 299–306.
- [9] N.T. Obee, O.S. Hay, *Environ. Sci. Technol.* 31 (1997) 2034–2038.
- [10] J.H. Cho, Y.J. Eom, S.H. Jeon, T.G. Lee, *J. Ind. Eng. Chem.* 19 (2013) 144–149.
- [11] J.H. Cho, Y.J. Eom, T.G. Lee, *J. Air Waste Manag. Assoc.* 62 (2012) 1208–1213.
- [12] C.Y. Tsai, T.H. Kuo, H.C. Hsi, *Int. J. Photo Energy* (2012), <http://dx.doi.org/10.1155/2012/874509>.
- [13] J. Wu, C.E. Chao, X.Y. Zhao, Q. Wu, X.M. Qi, X.T. Chen, Y. Cao, *Appl. Catal. B Environ.* 176–177 (2015) 559–569.
- [14] C.Y. Tsai, H.C. Hsi, T.H. Kuo, Y.M. Chang, J.H. Liou, *Aerosol Air Qual. Res.* 13 (2013) 639–648.
- [15] H.Z. Shen, I.R. Ie, C.S. Yuan, C.H. Hung, W.H. Chen, J.J. Luo, Y.H. Jen, *J. Hazard. Mater.* 289 (2015) 235–243.
- [16] C. Bechinger, G. Oefinger, S. Herminghaus, *J. Appl. Phys.* 7 (1993) 4527–4533.
- [17] L.L. Cao, J. Yuan, M.X. Chen, W.F. Shangguan, *J. Environ. Sci.* 22 (2010) 454–459.
- [18] J. Engweiler, J. Harf, A. Baiker, *J. Catal.* 159 (1996) 259–269.
- [19] M. Kobayashi, K. Miyoshi, *Appl. Catal. B Environ.* 72 (2007) 303–311.
- [20] Y. Yuan, Y.C. Zhao, H.L. Li, Y. Li, X. Gao, C.G. Zheng, J.Y. Zhang, *J. Hazard. Mater.* 227 (2012) 427–435.
- [21] C.Y. Tsai, H.C. Hsi, H.L. Bai, K.S. Fan, C.C. Chen, *J. Nanopart. Res.* 13 (2011) 4739–4748.
- [22] H.C. Hsi, C.Y. Tsai, *Chem. Eng. J.* 191 (2012) 378–385.
- [23] A. Khan, L. Sajjad, S. Shamaila, B.Z. Tian, F. Chen, J.L. Zhang, *Appl. Catal. B Environ.* 91 (2009) 397–405.
- [24] S.S. Chen, H.C. Hsi, S.H. Nian, C.H. Chiu, *Appl. Catal. B Environ.* 160 (2014) 558–565.
- [25] Y.R. Do, W. Lee, K. Dwight, A. Wold, *J. Solid State Chem.* 108 (1994) 198–201.
- [26] M.H. Kim, S.W. Ham, J.B. Lee, *Appl. Catal. B Environ.* 99 (2010) 272–278.
- [27] B.A. Dranga, H. Koeser, *Appl. Catal. B Environ.* 166 (2015) 302–312.
- [28] M.Y. Song, Y.K. Park, J.S. Jurng, *Powder Technol.* 231 (2012) 135–140.
- [29] H. Ohsaki, Y. Tachibana, A. Hayashi, A. Mitsui, Y. Hayashi, *Thin Solid Films* 351 (1999) 57–60.
- [30] L. Chen, M.E. Graham, G.H. Li, K.A. Gray, *Thin Solid Films* 3 (2006) 1176–1181.
- [31] C.C. Lo, C.H. Hung, C.S. Yuan, J.F. Wu, *Sol. Energy Mater. Sol. Cells* 91 (2007) 1765–1774.
- [32] A.S. Robert, M. Howard, *Anal. Chem.* 29 (1957) 760–761.
- [33] X.Q. Wang, S. Lasse, R. Su, S.F. Wendt, P. Hald, A. Mamakel, C.X. Yang, Y.D. Huang, B.B. Iversen, F. Besenbacher, *J. Catal.* 310 (2014) 145–156.
- [34] M. Anpo, T. Shima, S. Kodama, Y. Kubokawa, *J. Phys. Chem.* 91 (1987) 4305–4310.
- [35] B. Catherine, P. Biswas, *J. Catal.* 212 (2002) 145–156.
- [36] M.A. Henderson, *Surf. Sci. Rep.* 66 (2011) 185–297.
- [37] S. Liu, N. Jaffrezic, C. Guillard, *Appl. Surf. Sci.* 5 (2008) 2704–2709.
- [38] H.M. Yang, R.R. Shi, K. Zhang, Y.H. Hu, A.D. Tang, X.W. Li, *J. Alloys Compd.* 398 (2005) 200–202.
- [39] I.A.D. Castro, W.A. Jr, C. Ribeiro, *Cyst. Eng. Comm.* 16 (2014) 1514–1524.
- [40] T. Tokunaga, T. Kawamoto, K. Tanaka, N. Nakamura, Y. Hayashi, K. Sasaki, K. Kuroda, T. Yamamoto, *Nanoscale Res. Lett.* 7 (2012) 85–91.

- [41] T. He, Y. Ma, Y.A. Cao, X.L. Xu, H.M. Liu, G.J. Zhang, W.S. Yang, J.N. Yao, *J. Phys. Chem. B* 106 (2002) 12670–12676.
- [42] S. Higashimoto, M. Sakiyama, M. Azuma, *Thin Solid Films* 503 (2006) 201–206.
- [43] Y.T. Kwon, K.Y. Song, W.I. Lee, G.J. Choi, Y.R. Do, *J. Catal.* 191 (2000) 192–199.
- [44] Y.P. He, Z.Y. Wu, L.M. Fu, C.R. Li, Y.M. Miao, L. Cao, H.M. Fan, B.S. Zou, *Chem. Mater.* 15 (2003), 4309–4045.
- [45] X.Z. Li, F.B. Li, C.L. Yang, W.K. Ge, *J. Photochem. Photobiol. A Chem.* 141 (2001) 209–217.
- [46] B. Grbic, N. Radic, S. Stojadinovic, R. Vasilic, Z. Dohcevic-Mitrovic, Z. Saponjic, P. Stefanov, *Surf. Coat. Technol.* 258 (2014) 763–771.
- [47] JEOL, *Handbook of X-ray Photoelectron Spectroscopy*, JEOL, 1991.
- [48] H. Tang, H. Berger, P.E. Schmid, F. Levy, *Solid State Commun.* 87 (1993) 847–850.
- [49] K. Fujihara, S. Izumi, T. Ohno, M. Matsumura, *J. Photochem. Photobiol. A Chem.* 132 (2000) 99–104.
- [50] K.Y. Jung, S.B. Park, M. Anpo, *J. Photochem. Photobiol. A Chem.* 170 (2005) 247–252.
- [51] A. Suriawong, M. Smallwood, Y. Li, Y. Zhuang, P. Biswas, *Aerosol Air Qual. Res.* 9 (2009) 394–403.
- [52] Y. Li, D.P. Murphy, C.Y. Wu, K.W. Powers, J.C. Bonzongo, *Environ. Sci. Technol.* 42 (2008) 5304–5309.
- [53] A.W. Adamson, *Physical Chemistry of Surfaces*, 6th ed., John Wiley & Sons, New York, 1997, pp. 603–605, Chapter 17.
- [54] H.L. Li, C.Y. Wu, Y. Li, J.Y. Zhang, *Appl. Catal. B Environ.* 111–112 (2012) 381–388.
- [55] W. Gao, Q.C. Liu, C.Y. Wu, H.L. Li, Y. Li, J. Yang, G.F. Wu, *Chem. Eng. J.* 220 (2013) 53–60.
- [56] G. Snider, P. Ariya, *Chem. Phys. Lett.* 491 (2010) 23–28.
- [57] Y. Li, C.Y. Wu, *Environ. Eng. Sci.* 24 (2007) 3–12.
- [58] S.A. Negreira, J. Wilcox, *J. Phys. Chem.* 117 (2013), 24397–24336.
- [59] Y. Li, P. Murphy, C.Y. Wu, *Fuel Process. Technol.* 89 (2008) 567–573.
- [60] M. Imanari, Y. Watanabe, *Stud. Surf. Sci. Catal.* 7 (1981) 841–851.
- [61] H.L. Li, C.Y. Wu, Y. Li, J.Y. Zhang, *Environ. Sci. Technol.* 45 (2011) 7394–7400.
- [62] Y. Li, C.Y. Wu, *Environ. Sci. Technol.* 40 (2006) 6444–6448.
- [63] S. He, J.S. Zhou, Y.Q. Zhu, Z.Y. Luo, M.J. Ni, K.F. Cen, *Energy Fuels* 23 (2009) 253–259.
- [64] N.Q. Yan, W.M. Chen, J. Chen, Z. Qu, Y.F. Guo, S.J. Yang, J.P. Jia, *Environ. Sci. Technol.* 45 (2011) 5725–5730.